RSC Advances



REVIEW

View Article Online
View Journal | View Issue



Cite this: RSC Adv., 2024, 14, 36816

A timely update on g-C₃N₄-based photocatalysts towards the remediation of Cr(v₁) in aqueous streams

Sambhu Prasad Pattnaik, Upali Aparajita Mohanty and Kulamani Parida 🕩 *

Hexavalent chromium ($Cr(v_1)$) is a prominent carcinogen. In environmental engineering, the elimination of hexavalent chromium from aqueous media is a noteworthy field of study. In this regard, nanoparticle science and technology have contributed significantly to the photocatalytic reduction of $Cr(v_1)$. In this review, a methodical search was undertaken to discover the most recent advancements in the field of photocatalytic reduction of $Cr(v_1)$ utilizing $g-C_3N_4$ and composites derived from it. This paper deals with the advancements and applications of $g-C_3N_4$ and its composites in the $Cr(v_1)$ remediation of waterborne pollutants. Different intriguing systems, suggested by various researcher groups, have been discussed. Different characterization techniques often conducted on photocatalysts based on $g-C_3N_4$ have also been highlighted so as to gain an understanding of the $Cr(v_1)$ removal process. Lastly, the future scope of the $g-C_3N_4$ -derived photocatalysts, present challenges, and the viability of employing these photocatalysts in an extensive treatment plant have been discussed.

Received 13th October 2024 Accepted 30th October 2024

DOI: 10.1039/d4ra07350a

rsc li/rsc-advances

Introduction

Aquatic heavy metal pollution in recent decades has remained challenging for the industrialized world. Effluents from steel production, electroplating and leather tanning industries carrying chromium-containing wastewater find their way into the water bodies. Among the various existing oxidation states of chromium, hexavalent chromium is the most toxic and wellits carcinogenicity, teratogenicity, mutagenicity. 1-3 In the list of various toxic substances compiled by the ATSDR (Agency for Toxic Substances and Disease Registry) of the United States Department of Health and Human Services, Cr(v_I) occupies a significant place at 17th.⁴ If Cr(v_I) comes in contact with blood, it has the potential to form a stable Cr-hemoglobin complex and can stay in the bloodstream for about 120 days,5,6 impacting health. Because of its toxicity, the threshold value of Cr(vI) concentration in wastewater prior to discharge outside the plant boundary is fixed below 0.05 mg L^{-1} by regulatory authorities in many countries.7 This statutory requirement necessitates the treatment of wastewater until the limit of Cr(vi) concentration is maintained below 0.05 mg L⁻¹ before releasing it to the water bodies. Cr(v1) is not biodegradable, and therefore, the necessity for its degradation is quite thought-provoking from an environmental point of view. Various methods have been investigated regarding the

Centre for Nano Science and Nano Technology, Institute of Technical Education and Research, Siksha 'O' Anusandhan (Deemed to be University), Bhubaneswar, 751030, India. E-mail: kulamaniparida@soa.ac.in; sp1pattnaik@gmail.com; Tel: +919776645909: +919437647766

eradication of Cr(vi) present in wastewater, with the preferred method being adsorption. However, the ability of various adsorbents is hindered by their limited adsorption and many more challenges, like the cost associated with chemicals and release of secondary pollutants. Currently, there is a shift of attention towards an eco-friendly method for reducing hexavalent chromium via the utilization of semiconducting photocatalysts. The graph presented in Fig. 1 displays the number of research papers published in recent years in the arena of photocatalytic hexavalent chromium reductions.

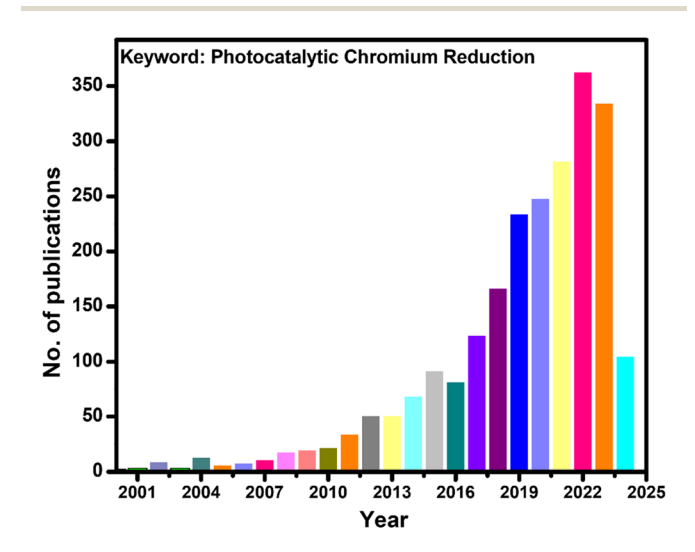


Fig. 1 Schematic showing the number of published articles on photocatalytic chromium(vi) reduction in the last twenty-four years.

Review RS

Photocatalysts that convert renewable solar energy into chemical energy are widely used in CO2 reduction, H2 generation, nitrogen fixation, chromium reduction,8-12 organic compound degradation and sterilization of potable water.13 Cr(vi) reduction through photocatalysis has garnered profound attention as photocatalysis employs sunlight as the energy source and abundant H2O and O2 as raw materials without generating any harmful by-products. Prior studies have extensively demonstrated profuse photocatalytic semiconductor materials in terms of Cr(vI) reductions such as (TiO2, g-C3N4 and other photocatalysts). Among the extensively studied and popular photocatalysts towards Cr(v1) remediation, it is found that while TiO2 offers more energetic UV-driven photocatalysis along with high catalyst surface area, it suffers from demerits like wide bandgaps, low absorption of visible-light spectrum and significant charge carrier recombination. Similarly, another photocatalyst that works well with both UV and visible radiation is ZnO, with the limitation of charge carrier recombination and surface defects affecting performance. Ag₃PO₄ exhibits high photocatalytic efficiency but is prone to photo corrosion and impaired by its limited visible light absorption. Bi₂WO₆ shows good activity for Cr(vi) reduction but has issues like low visible light absorption and possible reactive catalyst surfaces. CdS, as an effective visible-light photocatalyst, demonstrated low visible-light absorption, higher electron-hole recombination and toxicity concerns. On the other hand, versatile g-C₃N₄ demonstrated unique selectivity, visible-light absorption and no toxicity issues. Some demerits remain with the pristine material, like low specific surface area, low quantum efficiency and charge carrier recombination, all of which could be taken care of with appropriate strategies like compositing with other materials. Compared to other photocatalysts, g-C₃N₄ has merits in terms of photon wavelengths of approximately 460 nm conforming to its bandgap energy, making it well matched to visible light response, well represented in Fig. 2.

In addition, its grid structure containing heptazine and s-triazine rings with delocalised π electrons is favourable for electron and hole transport. g-C₃N₄, being an organic semi-conductor, has room for easy modification and alteration of energy levels by incorporating heteroatoms. Since the discovery of g-C₃N₄'s capability to catalyse water decomposition in 2009 by Wang and coworkers, 15 it has grabbed wide attention for its

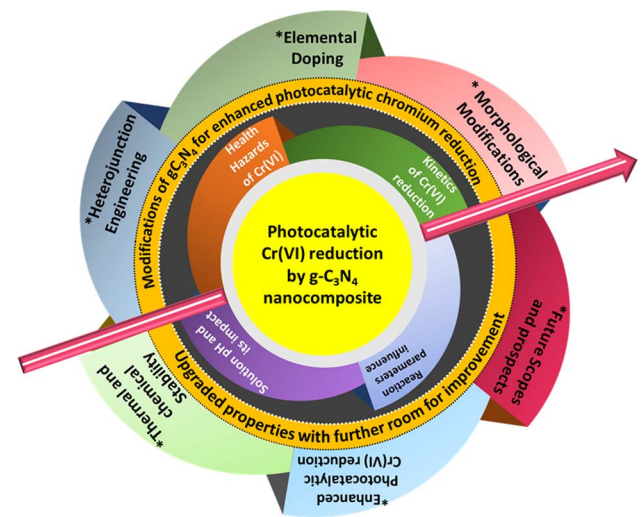


Fig. 3 Schematic illustration of the content of the review article.

excellent photocatalytic efficiencies. As a result, g- C_3N_4 -derived composites have found substantial application in photocatalysis, including chromium(v_1) reduction.

So far as Cr(vi) reduction in aqueous media by photocatalysis is concerned, there exists space for improvement in targeted chromium reduction efficiency essential for real-world applications, and consistent efforts need to be dedicated to the modification and development of PC. As the assessment of g-C₃N₄ continues to advance in a fast-paced manner, inclusive reviews and surveys are vital for staying abreast of the newest improvements across various aspects of this material, indispensable for the future. In favour of this, there is a demand for a timely and comprehensive review concerning the latest advances of g-C₃N₄ functionalization strategies towards photocatalytic reduction of Cr(vi). Herein, a run-through on g-C3N4 modified photocatalytic nano-heterostructures for the photocatalytic Cr(vI) reduction is well served. The review presents insights into the potential toxicity of Cr(v1) invasion in wastewater and follows it with the impressive photocatalytic properties of g-C₃N₄ and various modifications for dealing with critical edge chromium(vi) reduction. Furthermore, this review intends to provide the know-how in the area of g-C₃N₄ modification

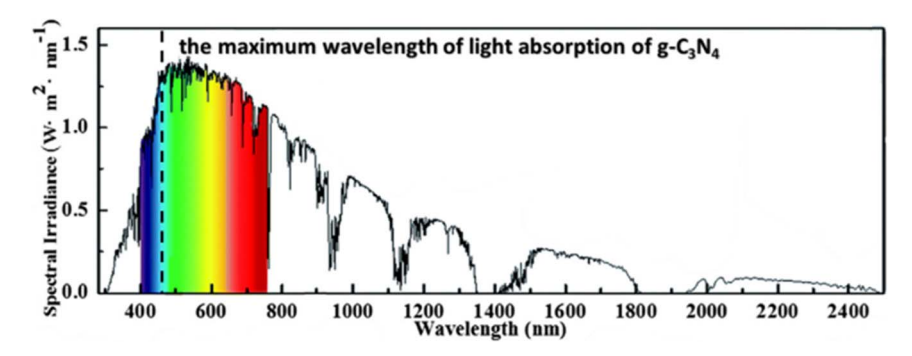


Fig. 2 Schematic exhibiting the maximum wavelength of light absorption of $g-C_3N_4$. Reproduced with permission from ref. 14, Copyright 2023, Elsevier.

strategies and motivate the researchers to attempt new alteration routes for $g\text{-}C_3N_4$ for efficient photoreduction of $Cr(v_1)$. The schematic representation of the content of the review is presented in Fig. 3.

Principle of photocatalytic Cr(vi) reduction

Exposure to humans and health issues linked to Cr(v1)

Hexavalent chromium has been considered to be in a heightened toxic oxidation state compared to its trivalent counterpart, owing primarily to the excellent capability of easy cellular membrane permeability. In this case, two oxyanions are predominantly formed in water in the presence of protons, $\text{CrO}_4^{\ 2^-}$ and $\text{CrO}_7^{\ 2^-}$, which undergo reversible reactions [eqn (1)].

$$2CrO_4^{2-} + 2H_3O^+ \leftrightarrow CrO_7^{2-} + 3H_2O$$
 (1)

Cr(vI) seamlessly undergoes reduction to the Cr(III) state just after entering the cell membrane, which leads to complex formation with intracellular macromolecules, including genetic materials.¹⁷ Cr(v_I) easily permeates through the cell membranes by forming free radicals, which cause DNA alterations and can subsequently lead to birth defects and reduced reproductive health (Chen et al., 2019).18 The intracellular Cr(vI) reduction can interact with DNA, producing genotoxic effects, altered immunological responses, and interrupted signalling pathways. 19 Additionally, Cr(vI) is recognised as a deadly carcinogen and teratogen causing skin abnormalities.20 Potential threats to plants are also caused by the presence of Cr(v1), which interferes in the process of photosynthesis by decreasing nutrient uptake.21 Various biochemical processes are also affected, generating reactive oxygen species in plant tissues and causing toxicity like chlorosis and necrosis.22

Kinetics of the Cr(vi) reduction process

Investigating the kinetics governing the reaction mechanism during the degradation of contaminants helps in our understanding of pollution abetment. The photocatalytic $Cr(v_I)$ reduction reaction invariably starts with the adsorption of $Cr(v_I)$ on the photocatalyst (PC) surface, after which it undergoes photoreduction. In order to comprehend the photocatalytic efficiency of $Cr(v_I)$ reduction, the frequently employed method is the Langmuir Hinshelwood pseudo 1st order model. The adsorption rate as a function of different factors is presented in [eqn (2)].

$$R = K'\theta = -\frac{\mathrm{d}c}{\mathrm{d}r} = k\left(\frac{kc}{1+kc}\right) \tag{2}$$

Here, R represents the rate of reduction, k represents the reduction rate constant, c represents the concentration of the contaminants, K' is the adsorption coefficient and θ represents the reactant site coverage. Additionally, for the lower concentration solution, the L–H model follows pseudo 1st order rate kinetics by eqn (3) and (4).

$$-\frac{\mathrm{d}C}{\mathrm{d}t} = -K_1C\tag{3}$$

$$\ln \frac{C}{C_0} = -K_1 t \tag{4}$$

 K_1 is the pseudo-first-order rate constant, t represents the time of reaction, and C and C_0 are the final and initial concentrations of the contaminant, in that order.

When light falls on a semiconducting material, it absorbs light and if the energy of the absorbed photon is more than the semiconductor bandgap, then the photocatalytic mechanism is initiated. Consequently, electrons in the semiconductor's valence band get excited to its conduction band, creating holes in the valence band. The photocatalytic reduction of Cr(vI) is caused by photoinduced electrons on the conduction band (C_B) of the semiconductor. The feasibility of Cr(v1) reduction is dictated by a condition that the conduction band edge has to be at a higher negative potential than the Cr(v_I)/Cr(_{III})/s redox potential. This requirement is normally fulfilled by the chosen semiconductor. As Cr(III)/Cr(0) demonstrates a higher negative redox potential, the reduction of Cr(vI) to the metallic state is not possible, i.e., (Cr(0)) by photocatalysis. The photogenerated electrons may move directly to the adsorbed Cr(v1) or to the photocatalyst's surface boundary. The movement of electrons from C_B to Cr(v_I) can happen in two possible ways.^{23,24} It is possible that Cr(vi) could be directly reduced to Cr(iii) by a single-step transfer involving three electrons from the C_B of the photocatalyst as per eqn (5). This mechanism appears to be more probable when there are hole scavenger molecules available in the medium, enhancing the charge separation of electrons and holes and leading to more electrons being available for the reaction.25 On the other hand, Cr(v1) is photoreduced through three sequential single electron transfers and obviously a very slow process as per eqn (6), producing intermediates of Cr(v) and Cr(v).26,27 As seen in eqn (5), the photoreduction of Cr(vi) utilizes H⁺ ions, preferring an acidic medium. The possibility of unwanted reverse reactions, i.e., Cr(III) oxidizing to Cr(vI) by oxidative positive holes and reactive oxidative species (ROS) on the surface of the photocatalyst, cannot be ruled out as per eqn (7). It is always preferred to add hole scavenger molecules in the aqueous medium so that they can react with oxidative species like positive holes and ROSs.28 The effectiveness of the photocatalytic reduction process depends on the properties of hole scavenger molecules used.29,30

$$Cr_2O_7^{2-} + 14H^+ + 6e^- \rightarrow 2Cr^{3+} + 7H_2O$$
 (5)

$$Cr(vi) + e^- \rightarrow Cr(v) + e^- \rightarrow Cr(iv) + e^- \rightarrow Cr(iii)$$
 (6)

$$Cr(III) + ROSs \rightarrow Cr(VI)$$
 (7)

$$O_2 + e^- \to *O_2^-$$
 (8)

$$*O_2^- + Cr(v_1) \to Cr(v) + O_2$$
 (9)

$$HCrO_4^- + 7H^+ + 3e^- = Cr^{3+} + 4H_2O$$
 (10)

 $E_{hv} > E_g \qquad e^- \qquad e$

Review RSC Advances

Fig. 4 Schematic showing the photochemical chromium(vi) reduction process

$$CrO_4^{2-} + 4H_2O + 3e^- = Cr(OH)_3 + 5OH^-$$
 (11)

In a pure aqueous medium, free of hole scavenger molecules, the photogenerated *O_2 on the C_B can go for the reduction of Cr(vi) to Cr(v) in eqn (8)–(11). 31,32 However, in real-life situations, chrome-laden aqueous streams do contain organic contaminants that work as hole scavengers. A pictorial illustration of the photocatalytic reduction of hexavalent chromium procedures using semiconducting photocatalysis is displayed in Fig. 4.

Influence of reaction parameters

Factors influencing $Cr(v_I)$ photocatalytic reduction include types of light sources and intensities thereof, presence of hole scavengers, initial $Cr(v_I)$ concentration, pH of the medium and catalyst dosage. The source of light governs the light intensity and frequencies of emitted radiations, *i.e.*, the quality and quantities of photons released. The photon should be capable of knocking off electrons in the V_B of the semiconductor PC to its conduction band. The more energetic the photon, the better it is. Photons with lesser energy than PC's band gap are of no use. Similarly, a higher number of useful photons from intense beams commits a higher number of photoinduced electrons for participation in photocatalysis.

While electrons in the C_B participated in photocatalysis to provide meaningful reaction products, at the same time, holes, a highly oxidising species in the V_B , remain in the absence of a scavenger. In order to drive the reaction forward unhindered, the holes need to be consumed in the overall reaction or scavenged out by using a hole scavenger, failing which will hinder the overall photocatalytic process. Thus, we can see that the hole scavenger impacts the photocatalytic process considerably. The initial $Cr(v_I)$ concentration denoted by C_0 is a critical parameter. The photocatalytic reaction efficiency depends on it when other conditions remain unaltered. At lower C_0 , the PC effect is more pronounced. The solution pH is a crucial factor for $Cr(v_I)$ reduction as the reaction is facilitated by lower pH. The PC concentration impacts the photocatalytic reaction. For

a given photocatalyst, say in this case, g- C_3N_4 composite and initial chromium concentration of C_0 , the catalyst dose requires to be optimised for a given light source of particular intensity as more catalyst dosage beyond a certain limit (to be determined experimentally) may cause decrease in the photocatalytic degradation rate due to increase in the turbidity of the reaction medium and consequent decrease in light intensity in the reaction medium, which in turn causes lower light absorption by the photocatalyst.

The presence of organic materials in rejected water streams plays a crucial role in the photocatalytic degradation of $Cr(v_I)$. In fact, the $Cr(v_I)$ bearing wastewater streams, in reality, contain organic matter as well. At times, these materials are oxidized on the catalyst surface, consuming photogenerated holes and acting as a scavenger for holes that help boost the photocatalytic degradation of $Cr(v_I)$. That is why many research publications describe $Cr(v_I)$ photocatalytic reduction and simultaneous oxidation of the organic matter together.

Solution pH and its impact

The pH of the aqueous medium is a very important aspect in deciding the rate of the photocatalytic reduction of Cr(vi) as H^+ ions participate in the overall reaction process. Due to electrostatic interactions, the protons also help pull the photoinduced electrons from the C_B of PC to the media containing Cr(vi). Hence, an acidic medium always favours the photocatalytic reduction of Cr(vi) and is almost negligible at an alkaline pH.^{29,33}

Physicochemical propertied of g-C₃N₄

Over the years, g-C₃N₄, owing to its 2-D π conjugated polymeric, narrow band gap, and metal-free semiconductor characteristics, has emerged as an eye-catching material for various applications in the fields of sensors, supercapacitors, adsorptions and photocatalytic redox reactions. The physicochemical characteristics of g-C₃N₄ play a pivotal in the photocatalysis avenue, while another essential property of g-C₃N₄ is stability. g-C₃N₄,

RSC Advances Review

with significant thermal stability, allows this material to be utilized in high-temperature reactions. In addition to its thermal stability up to 600 °C, g-C₃N₄ also possesses good chemical stability across a varied pH range, i.e., immune to acids and alkalis. 34,35 The higher negative displacements of zeta potential provide better stability in aqueous solutions debarring agglomerations. The easy-to-exfoliate layered structure of g-C₃N₄, along with various functional amino and imino groups, enhances its dispersibility, providing enhanced active sites for interactions during the reactions. Among a plethora of sustainable next-gen photocatalysts, nanostructured g-C₃N₄ occupies a prominent place. This polymeric, metal-free photocatalyst has a graphitic planar structure consisting of conjugated tris-s-triazine rings in abundance. Its structure provides sufficient π bonded electrons excitable on absorbing visible radiation. Due to this, it exhibits sensitivity to the visible range of solar light thanks to its visible light-driven band gap and appropriate band edges. 36-38 g-C₃N₄ is easy to prepare at low cost from precursors rich in earth-abundant materials like nitrogen and carbon. It can be prepared from precursors rich in contents of carbon and nitrogen, such as urea,39-44 melamine45-55, cyanamide,56-59 dicyandiamide,60-63 ammonium thiocyanate,64 and thiourea.65-67 As the band gap of g-C3N4 is 2.7 eV, it can effectively absorb visible radiation of less than 450 nm wavelength, implying future prospects in solar energy utilization applications. Besides these, it is nontoxic in nature eliminating the need of handling issues. The photocatalyst is easy to separate and amenable to recycle and reuse.

In spite of the advantages of g-C₃N₄ as a photocatalyst, certain inherent bottlenecks⁶⁸ hinder the performance of pristine g-C₃N₄ towards practical use to date. This is partly because standard synthesis methods of thermal poly-condensation of precursors produce relatively thick materials consisting of stacked s-triazine layers. The stacking of s-triazine layers creates bulk g-C₃N₄ materials with low specific surface areas. Lower SSA leads to fewer available reaction sites, impeding the photocatalytic reaction kinetics. Other bottlenecks in the photocatalytic activity of g-C₃N₄ include different factors, such as fast photogenerated charge carrier recombination,69 poor crystallinity and surface defects. Researchers, to this day, have been working on optimizing synthesis techniques of g-C₃N₄ to modify its physicochemical properties and photocatalytic efficiency. The design and fabrication of g-C₃N₄ composites of suitable band structure could improve the charge separation efficacy, thereby enhancing the photocatalytic performance. Hence, the majority of work in this field of research is devoted to the construction of suitable g-C₃N₄ derived composites with suitable band structure, increased porosity and surface area, enhancing its overall photocatalytic performance. A summarized representation of all the properties of g-C₃N₄ is given in Fig. 5.

Exfoliation of g- C_3N_4 is carried out to obtain nanosheets, which improve the SSA. The high energy conversion efficiency of g- C_3N_4 as a photocatalyst may be achieved by stimulating the efficient parting and migration of photoinduced charge carriers, expanding the spectral response range and increasing its specific surface area. All of these shortcomings of g- C_3N_4

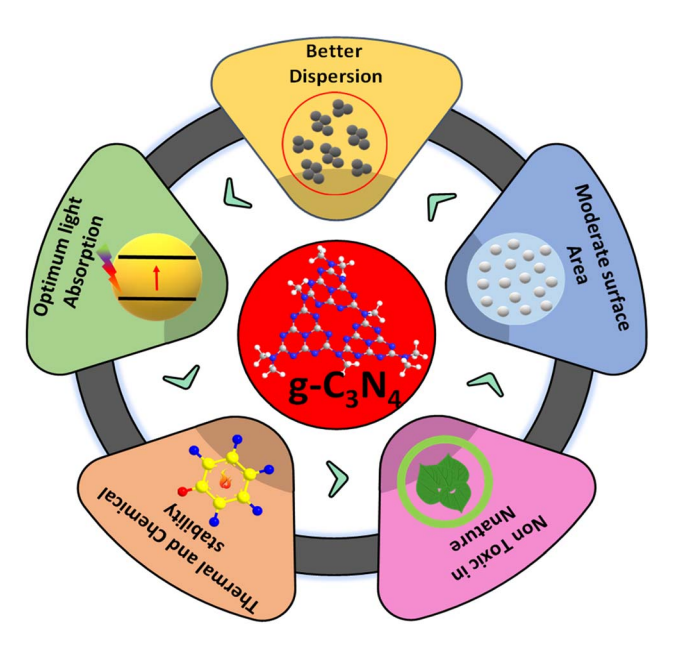


Fig. 5 Schematic displaying the properties of g-C₃N₄.

could be alleviated to some extent by doping foreign materials into the g- C_3N_4 matrix using copolymerization and other techniques to change the electronic and band arrangement of g- C_3N_4 . The heterojunctions made on g- C_3N_4 are an outcome of effective strategies^{70,71} to design and fabricate amalgamated photocatalysts. The g- C_3N_4 heterostructures distinctly enhance the photocatalytic performance of g- C_3N_4 by improving the parting and transfer of photoinduced charges, broadening the light absorption range, and widening redox potentials, attributable to the existence of both built-in electric fields at the g- C_3N_4 interface and other material-making composites and the complementarity between the g- C_3N_4 electronic structure and that of the constituent material. Doping with impurities such as metals, nonmetals or nanoparticles also helps lower the recombination efficiency of photoinduced e^- - h^+ pairs.

Modification of $g-C_3N_4$ for promoting $Cr(v_1)$ reduction

Heterojunction formation

The g- C_3N_4 heterojunction catalyst is synthesized by combining g- C_3N_4 layers with layers of other materials like semiconductors so that an interface between the two layers may be created. The g- C_3N_4 heterojunction is always beneficial compared to pristine g- C_3N_4 in photocatalytic applications. The heterojunction reduces the recombination of charge carriers on the interface and thereby improves the photocatalytic activity of a PC.

Nguyen *et al.* reported⁷² that the g- C_3N_4 and n-p type ZnO/BiOBr heterojunction resembling a flower was synthesized using a hydrothermal method, with the potential for Cr(vI) removal in aqueous media. They determined the phase structures and catalyst purity from the XRD patterns of pristine ZnO, pristine BiOBr, pristine g- C_3N_4 , and the BiOBr/ZnO heterojunction, as shown in Fig. 6a. The optimal PC with catalyst

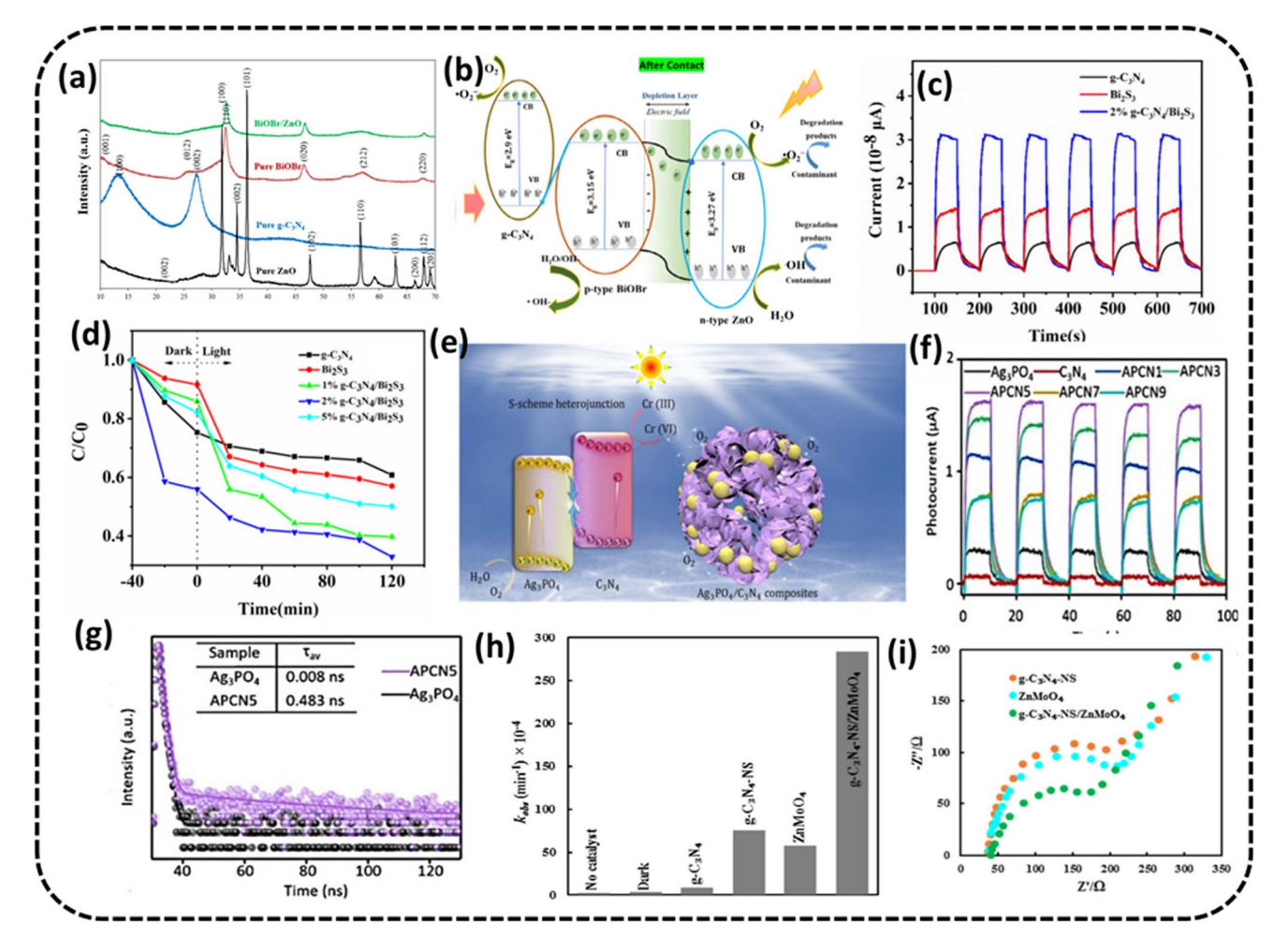


Fig. 6 (a) XRD analysis of ZnO, BiOBr, BiOBr/ZnO and $g-C_3N_4$ samples. (b) Schematic depicting the energy band structure of PCs after the formation of the ZnO/BiOBr heterojunction and probable mechanism of photocatalysis. Reproduced with permission from ref. 72 Copyright 2023, Elsevier. (c) Photocurrent response of pristine $g-C_3N_4$, Bi_2S_3 , and 2% $g-C_3N_4/Bi_2S_3$ (d) photocatalytic efficacy of Bi_2S_3 , $g-C_3N_4$, and 2% $g-C_3N_4/Bi_2S_3$: reduction of Cr(w) exposed to visible radiation. Reproduced with permission from ref. 73, Copyright 2022, Avanti Publishers. (e) Schematic of the Ag_3PO_4/C_3N_4 composite with S-scheme heterojunction (f) transient photocurrent responses (g) time-resolved PL decay spectra reproduced with permission from ref. 74 Copyright 2022, FJIRSM, CAS, Fuzhou (h) Cr(w) reduction rate over the prepared photocatalysts, (i) EIS curves for the fabricated photocatalysts Reproduced with permission from ref. 75 Copyright 2022, Springer Nature.

amounts of 0.05 g g-C₃N₄ and 0.4 g ZnO/BiOBr-2 (molar ratio Bi/ Zn = 2) were seen to accomplish 96% of Cr(vi) elimination in 180 min with measured rate constant = 0.0105 min⁻¹ under simulated UV light. The experiments were conducted with a C_0 = 10 mg L⁻¹ of Cr(vi) with a pH value of 2. The PC could be reused without loss of efficiency for four consecutive cycles, indicating its good photocatalytic stability. The improvement in performance was attributed to fewer recombining charge carriers at the boundary and a rise in the range of absorption of UV light. The well-presented schematic illustration of the reaction mechanism is presented in Fig. 6b.

Ding *et al.* synthesized $Bi_2S_3@g-C_3N_4$ Z-scheme heterojunctions⁷³ using the hydrothermal method. The optimal PC of 2% g- C_3N_4/Bi_2S_3 could reduce 10 mg L^{-1} Cr(v_I) solution to the tune of 93.4% in 120 min under simulated solar radiation, as displayed in Fig. 6c. The improved photocatalytic activity of PC was ascribed to a better segregation and movement of the

charge carriers, and its optimum band structure helped increase the range of light absorption.

The current trend of PC exposed to visible light reveals the separation efficiency of photoinduced charge carriers. The photocurrent responses of pristine g-C₃N₄, Bi₂S₃, and 2% g-C₃N₄/Bi₂S₃ are shown in Fig. 6d, where the photocurrent rises as mentioned: pristine g-C₃N₄ < Bi₂S₃ < 2% g-C₃N₄/Bi₂S₃, of which the photocurrent of optimal PC 2% g-C₃N₄/Bi₂S₃ is considerably more than that of pure g-C₃N₄ and Bi₂S₃. It was shown that the composite of g-C₃N₄ and Bi₂S₃ radically improved the separation rate of photoinduced charge carriers, leading to the enhancement of the photocatalytic redox rate of g-C₃N₄/Bi₂S₃ composites.

Yang et al. created an Ag₃PO₄/g-C₃N₄ heterojunction composite⁷⁴ by coupling Ag₃PO₄ particles with g-C₃N₄ hollow spheres via an in situ precipitation method. The S-scheme heterojunction amidst Ag₃PO₄ and g-C₃N₄ could hasten the charge segregation and improve the photoreduction ability, as can be

RSC Advances Review

predicted from the transient photo current response shown in Fig. 6e. The highest transient photocurrent response came from optimized PC APCN5, implying the best expected photocatalytic response, as displayed in Fig. 6e. Time-resolved PL decay spectra in Fig. 6f also corroborated the expectation from PC as the extended fluorescence lifetime of APCN5 implied boosted disassociation of photogenerated e^--h^+ pairs. The said g-C_3N_4 hollow sphere structure could accommodate a higher number of active sites in the photocatalytic process, resulting in an 87.9% reduction of a 20 mg L^{-1} initial Cr(v1) solution in 75 min under visible light using the optimized composite denoted as APCN5 having 5% carbon spheres.

Mousavi *et al.* fabricated a heterojunction⁷⁵ in which ZnMoO₄ was loaded on g-C₃N₄ nanosheets by a calcining-hydrothermal method and the resultant composite was shown to reduce Cr(vi) in 120 min with the rate constant of 284 min⁻¹, as presented in Fig. 6g. The EIS measurements revealed the separation efficiency and interfacial charge transfer resistance of PCs (Fig. 6h). The Nyquist plot of g-C₃N₄-NS/ZnMoO₄ possessed the smallest semicircle, implying the fastest movement of charge pairs, least recombination and predicted capability of more photoactivity for g-C₃N₄-NS/ZnMoO₄.The improved overall photocatalytic ability was credited to the

boosted visible-radiation absorbance and low rate of charge recombination. The PC could be used for four consecutive cycles.

Bankole et al. prepared Ag₂O-Ag₂CO₃/g-C₃N₄ p-n/n-n dual heterojunctions denoted by AAG.76 AAG utilized the mediation of atmospheric CO2 and could achieve >99.5% reduction of 10 ppm $Cr(v_1)$ solution at a catalyst concentration of 0.1 g L^{-1} in the presence of oxalic acid within 30 min irradiation to visible light, as shown in Fig. 7a. Upon exposure to visible light, electrons are evicted from the V_B of the semiconductors (Ag included) and transferred to their respective CB edges, and simultaneously, the holes with positive charges are created at the V_B edges. It is obvious from the band structures that the photoinduced electrons moved from high negative CB edges of p-Ag₂O, n-g-C₃N₄ and Ag to the least negative C_B of n-Ag₂CO₃. The highly reductive electrons accumulated on the CB of n-Ag₂CO₃ and were captured by HCrO₄⁻¹ (at lower pH values of OA) and reduced to Cr(III). Oxalic acid in the reaction medium used up the accumulated holes and hydroxyl radicals at the V_B of p-Ag₂O to generate highly reductive anion radicals of 'CO₂-, stopping the chances of the recombination of e⁻/h⁺ pairs and also reduced Cr(vI) to Cr(III) augmenting the overall

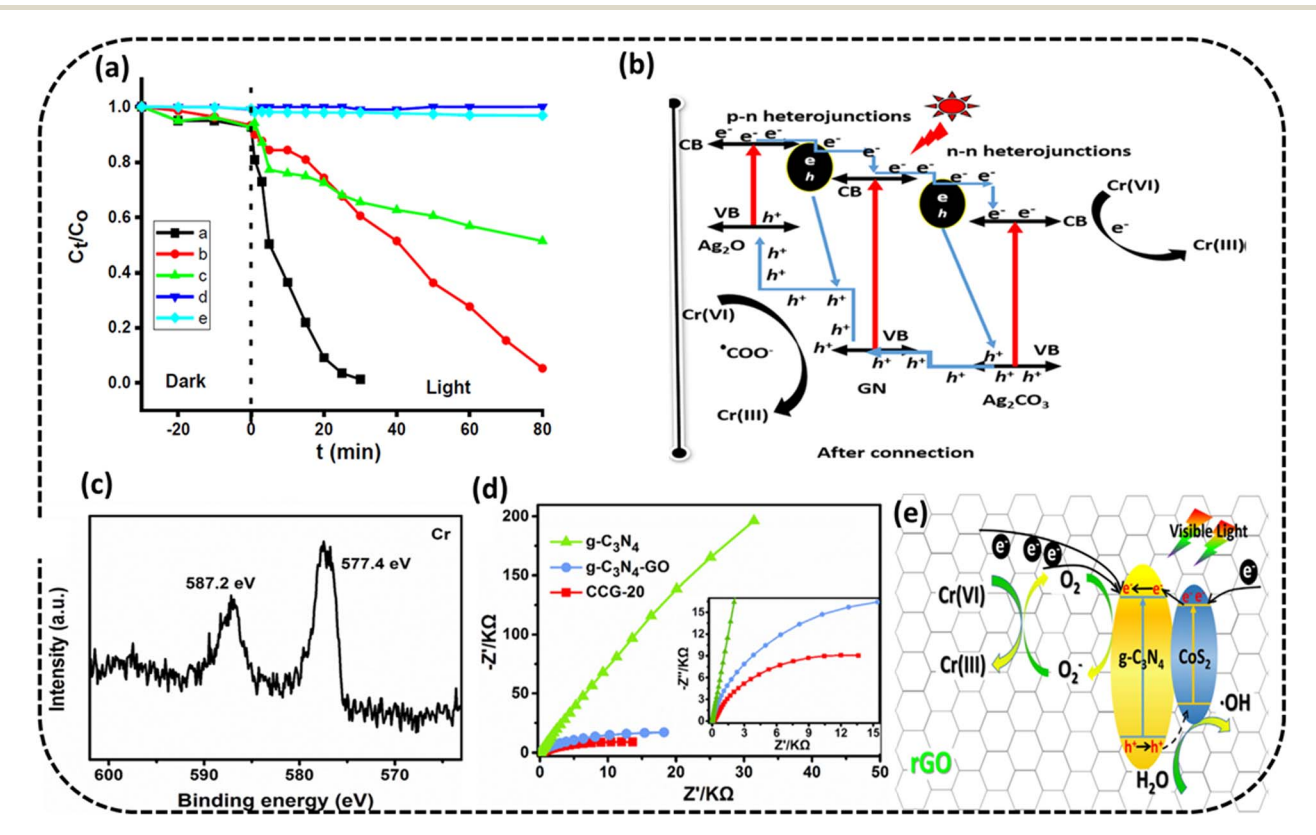


Fig. 7 (a) Photocatalytic $Cr(v_i)$ reduction to Cr(iii) using AAG with OA, AA with OA, $g-C_3N_4$ with OA, OA and without catalyst and photolysis only (b) energy band structures of the AAG $(n-Ag_2CO_3, p-Ag_2O)$ and $n-g-C_3N_4$) composite after band alignments to form p-n/n-n dual heterostructures for $Cr(v_i)$ photocatalytic reduction. Reproduced with permission from ref. 76. Copyright 2022, Elsevier (c) XPS spectra of $Cr(v_i)$ composite after band alignments to form $Cr(v_i)$ and $Cr(v_i)$ photocatalytic reduction. Reproduced with permission from ref. 76. Copyright 2022, Elsevier (c) XPS spectra of $Cr(v_i)$ photocatalytic reduction EIS plots for $Cr(v_i)$ and $Cr(v_i)$ photocatalytic reduction. Reproduced with permission from ref. 77. Copyright 2020, Elsevier.

photocatalytic process, as shown in Fig. 7b. The PC could be used for five consecutive cycles.

Wang et al. fabricated the CoS₂/g-C₃N₄ heterostructure junction backed by rGO through a one-pot solvothermal method.⁷⁷ The improved photocatalysts could affect >99.8% removal efficiency for 20 mg L⁻¹ Cr(v_I) and a PC concentration of 500 mg L⁻¹ under 120 min at low pH of 2 and still exhibit greater than 98% reduction efficiency, following five cycles in the same state. From the EIS plots, it is obvious that the charge transfer efficiency of the ternary nanocomposite CoS₂/g-C₃N₄rGO could be the best, indicating its excellent photocatalytic performance presented in Fig. 7c. The increased photocatalytic activity of the CoS₂/g-C₃N₄-rGO ternary nanocomposite could be attributed to the increased utilization of visible light because of the coupling effect in the hybrid nanocomposite and increased SSA with additional exposed active sites of CoS₂ scattered across rGO and the formed heterojunction of CoS₂/g-C₃N₄ along with the improved separation of photogenerated charge carriers. The e and superoxide radicals ('O2") were probable primary dynamic species during the reduction of Cr(vi) (Fig. 7d). Highresolution XPS spectra of Cr(III) 2p on the optimised photocatalyst surface CCG-20 after completion of the reduction reaction indicated Cr(vi) reduction to Cr(iii) (Fig. 7e).

Reddy *et al.* synthesized g-C₃N₄ operationalized yttrium-doped ZrO₂ hybrid heterostructured (g-C₃N₄YZr) nanoparticles for photocatalytic Cr(v₁) reduction. When g-C₃N₄ was doped with a small amount of ZrO₂, the light adsorption ability was markedly improved because of the thin band gap. The unique arrangement of g-C₃N₄YZr displayed a better reduction of photocatalytic Cr(v₁) because of its large surface area, lowered charge carrier recombination rate and revealed better photocatalytic activity after being exposed to sunlight for 90 minutes. The PC could withstand four repeatability tests, signifying its structural stability.

Mishra *et al.*⁷⁹ fabricated $Bi_4O_5I_2/g$ - C_3N_4 , p-n type direct Z-scheme heterojunction photocatalysts (BOCNs) with hierarchical 3D/2D architectures by a two-step solvothermal-calcination method. The optimised photocatalyst designated as BOCN3 exhibited Cr(vi) removal efficiency of 90.3% at a pH of 2.2 within 60 min, catalyst dose 0.4 g L^{-1} and an initial Cr(vi) concentration of 40 mg L^{-1} . The photocatalyst could be tested up to the fifth successive cycle without much change in photocatalytic activity, which indicated its improved stability and reusability.

Zhao et al.*0 synthesized the g-C₃N₄/C/Fe₂O₃ photocatalyst by securing g-C₃N₄ nanosheets onto C/Fe₂O₃ prepared using collagen fiber from biochar. The PC displayed improved Cr(vI) removal efficiency than pristine g-C₃N₄, and with the rise of Fe quantity in the g-C₃N₄/C/Fe₂O₃ photocatalyst, Cr(vI) reduction efficiency increased. The improved photocatalytic activity was credited to the indirect Z-scheme heterojunction formed amongst g-C₃N₄ and C/Fe₂O₃ that improved the separation efficiency of the light-induced charge carriers. The light-generated electrons (e⁻) were found to be the driving force for Cr(vI) removal.

Huo et al. fabricated the g-C₃N₄/BiFeO₃/carbon nanotube ternary composite⁸¹ using a hydrothermal synthesis method.

When the g-C₃N₄/BiFeO₃/CNT composite was utilized as a PC, the photocatalytic performance improved substantially by reducing the rate of recombination of e^-/h^+ pairs throughout the photocatalytic reduction reaction of Cr(vi). The extra CNTs served as conduits to speed up the electron transfer procedure. Because of the high surface area, there were more active sites, which improved the photocatalytic activity. The work's findings may offer a workable foundation for treating wastewater that includes heavy metals and organic contaminants. A 93% reduction efficiency could be achieved in the case of a 5 mg L⁻¹ of Cr(vi) solution in 5 h under visible irradiation.

Niu *et al.* fabricated $Ag_{32}NCs/g-C_3N_4$ and $Ag_9NCs/g-C_3N_4$ and hybrid nanocomposites⁸² by loading $Ag_{32}(MPG)_{19}$ and $Ag_9(-1200)_{19}$ nanoclusters (NCs) onto $g-C_3N_4$ utilizing a basic penetration technique to form $Ag_9-NCs/g-C_3N_4$ and $Ag_{32}NCs/g-C_3N_4$ hybrid nanocomposites. These photocatalysts could reduce 20 mg L^{-1} 100% Cr(vi) solution after 30 min and 50 min respectively under exposure to visible light. The PCs were stable enough to be recycled five times.

Chen *et al.* fabricated 3D g-C₃N₄@cellulose aerogels improved by cross-linked polyester fibers. ⁸³ Cellulose aerogels (CAs) with high permeabilities and SSA were used as a carrier for g-C₃N₄. As CA does not have sufficient strength and is susceptible to damage under the application of a slight force, particularly in water; therefore, the same was reinforced by blended polyester fibers (B-PET). In this case, CA with g-C₃N₄ nanosheet was supported by blended polyester fibers (B-PET), which increased the tensile strength of pure CA. 200 mg of PC could reduce $Cr(v_1)$ (2 × 10⁻⁴ mol L⁻¹) to the extent of 91% in 120 min under sunlight.

Morphological modification

The morphology of nanostructured g-C₃N₄ and its derivative is an important parameter from the photocatalytic standpoint. Morphology control of the g-C₃N₄ nanostructure appears to be a good idea as nanostructured g-C3N4 shows increased photocatalytic performance than bulk g-C3N4. Morphology alone can make a big difference to the photocatalytic activity of g-C₃N₄ and compounds derived from g-C₃N₄ as it controls the available redox reaction sites on the PC surface. g-C₃N₄ provides twodimensional (2D) sheets on exfoliation, which is comprised of tri-s-triazine structures mutually connected via tertiary amines; other nanostructures like nanotubes and nanoflowers are also widely studied. Because of these types of structures, it is possible to fabricate g-C₃N₄-based hybrid nanocomposites by joining g-C₃N₄ with other components. The nanocomposites based on g-C₃N₄ have clear advantages over the pure g-C₃N₄, such as outsized surface area, more separation time, more efficiency of transportation and adequate visible light absorption. The increase in the SSA and other characteristics improves the photocatalytic ability of PC by making available more surface area to adsorb the reactants, lower charge recombination rate and the consequent higher photoreduction of Cr(vI).

Yu et al. synthesized CA-g-C₃N₄, i.e., petal-like g-C₃N₄ embedded with citric acid (CA).⁸⁴ This treatment with CA changed the morphology and structure of the composite

RSC Advances Review

photocatalyst, enabling a more porous microstructure with a higher specific surface area and larger pore size, resulting in a rise in the number of active sites on its surface. The region of interaction between the photocatalyst and Cr(vi) was improved, causing the Cr(vi) degradation rate to 93% compared to 48% of pristine $g\text{-}C_3N_4$ under comparable circumstances (Fig. 8a). The morphology control of $g\text{-}C_3N_4$ could improve its photocatalytic activity, and the SEM image of $CA\text{-}g\text{-}C_3N_4$ is presented in Fig. 8b. The PC was stable enough to be recycled three times. The citric acid treatment effectively dispersed $g\text{-}C_3N_4$, increased the SSA of the photocatalyst, enhanced the number of active sites on the photocatalyst surface and thus enhanced the photocatalytic performance of the catalyst.

Jiménez-Flores *et al.* synthesized a g-C₃N₄/HAP composite by thermal condensation of melamine mixed with hydroxyapatite.⁸⁵ As seen from the SEM image, the morphology of the g-

C₃N₄/HAp combination exhibited a layered and piled structure common to g-C₃N₄ materials (Fig. 8c). The insert in the figure depicts the presence of nitrogen (65.63%), carbon (29.54%), phosphorus (0.59%), oxygen (2.39%), sodium (0.29%) and calcium (23.16%) in the g-C₃N₄/HAP composite. A mixture of heterogeneous phases maintaining the lamellar structure typical of pristine hydroxyapatite could be seen. Fig. 8d presents the simulated image of hydroxyapatite. The upsurge in the photocatalytic activity could be ascribed to a positive collaborative outcome created by the interaction between components, i.e., g-C₃N₄ and hydroxyapatite impacting the surface morphology leading to improved photocatalytic behavior, as reflected in the bar chart in Fig. 8e displaying the kinetic rate constant values for g-C₃N₄, hydroxyapatite and g-C₃N₄/HAp composite under exposure to visible light. The 100% reduction of 40 ppm Cr(vI) solution was achieved after 25 and 210 min

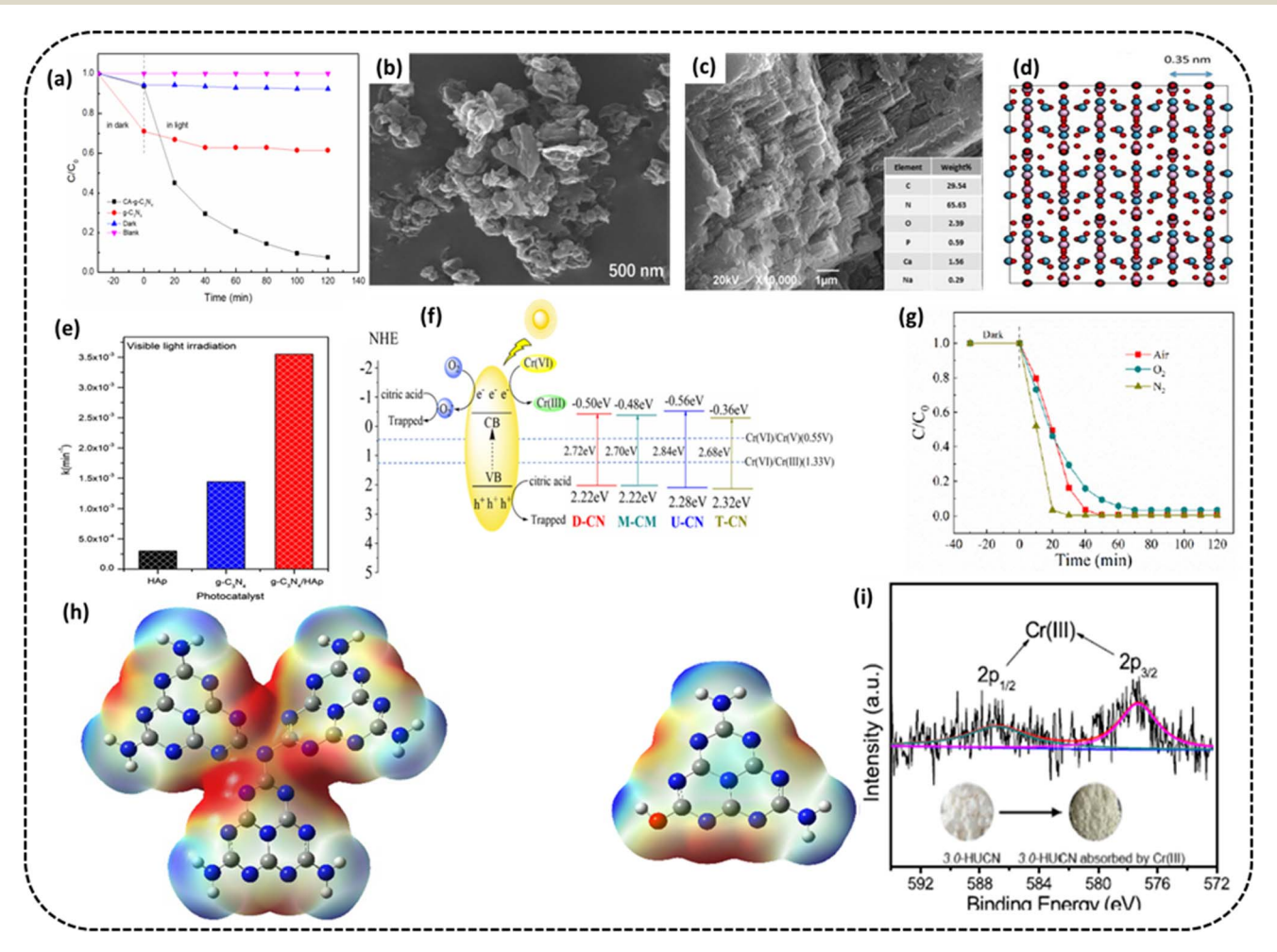


Fig. 8 (a) $Cr(v_1)$ removal rate on $g-C_3N_4$ and $CA-g-C_3N_4$ (b) SEM image after the reaction of $CA-g-C_3N_4$. Reproduced with permission from ref. 84, Copyright 2023, MDPI (c) SEM image of the $g-C_3N_4$ /HAp composite (d) structure simulation by using a zone axis [010] of hydroxyapatite $Ca_5(PO_4)_3(OH)$ (e) bar graph of reaction rate constant values for $g-C_3N_4$, hydroxyapatite, and $g-C_3N_4$ /HAp composite under exposure to visible radiation. Reproduced with permission from ref. 85, Copyright 2020, Elsevier (f) Proposed mechanism for photocatalytic $Cr(v_1)$ remediation over UCN (g) rate of photocatalytic remediation of $Cr(v_1)$ by UCN. Reproduced with permission from ref. 86, Copyright 2021, MDPI (h) ESP surface distribution of optimized UCN and HUCN model (i) XPS spectrum of $Cr(v_1)$ adsorbed on the 3.0-HUCN after photocatalytic reduction of $Cr(v_1)$. Reproduced with permission from ref. 87 Copyright 2020, Elsevier.

Review

exposure in case of UV and visible light in that order. The composite was stable enough to be tested for 8 consecutive cycles.

Sun *et al.* synthesized alkali-modified g-C₃N₄ (*c*OH-CN) and acid-modified g-C₃N₄ (*c*H-CN)⁸⁸ and reported 100% Cr(vI) could be removed in 60 min under visible radiation even though it merely demonstrated 30% in the case of the pure g-C₃N₄. The surface altered g-C₃N₄ by acid-base regulation demonstrated a larger surface area, increased pore structure abundance, a greater spectrum of visible radiation absorption, more band gap energy values, and greater ability to separate electron-hole pairs leading to efficient photocatalysis for Cr(vI) remediation.

Liang *et al.* developed a synthesis technique for $g\text{-}C_3N_4$ photocatalysts using urea, thiourea, dicyandiamide, and melamine as precursors. The varying band structure of $g\text{-}C_3N_4$ with separate morphologies derived from different precursors may be seen (Fig. 8f). The $g\text{-}C_3N_4$ derived from urea with nanosheet morphology, higher SSA, and more occupancy of surface amine groups demonstrated better than before photocatalytic activity. The morphology of the nanosheet and high surface area made it easier for charges to be separated and transmitted, which was beneficial for Cr(vi) reduction when exposed to white light irradiation. Photocatalytic remediation of Cr(vi) was made possible to the extent of 99.5% within 60 min using the urea-g- C_3N_4 experiment: Cr(vi) concentration at 50 mg L^{-1} , urea-g- C_3N_4 amount = 50 mg, volume = 150 mL, citric acid = 0.9 mM at pH = 3 when exposed to white light.

Wang et al. fabricated an interconnected open network of hydroxyl-altered g-C₃N₄, i.e., (HUCN)⁸⁷ using the hydrolysis of urea-derived g-C₃N₄, i.e., (UCN) in aqueous NaOH solution, after which self-assembly occurs via a dialysis process. In contrast to bulk g-C₃N₄, i.e., (UCN), numerous exposed active sites, a quick rate of separation of photoinduced e⁻/h⁺ pairs and a greater negative conduction band edge potential are just a few of HUCN's many advantages. These benefits give the HUCN, in comparison to UCN, a noticeably better capacity for photocatalytic remediation of aqueous Cr(v1) under exposure to artificial sunlight. These observations are in line with the theoretical prediction from DFT studies. The ESP distribution obtained from the DFT calculation for the optimized models of UCN and HUCN shows a realistic pathway for electron movement at the edge of PC. As displayed in Fig. 8g and h, the blue and red colors in ESP maps denote low-electron (positive potentials) and the electron opulent (negative potentials) regions, respectively. The electron-rich areas of UCN are situated at the bridged tertiary nitrogen atoms and triangular edge nitrogen atoms in melem units. On the other hand, the electron-deprived areas remain at the other chunks of melem units (Fig. 8g). During the course of hydrolysis, the -OH groups are hosted at the HUCN edges and receive holes, sparing more electrons found at the triangular edge N atoms of melem units (Fig. 8h). It is inferred that the reduction spots have a huge shift from the internal flat part of UCN to the HUCN edges. Considering the above findings, it is concluded that progressively diminished electrochemical impedance or increased photocurrent density indicates faster photoinduced e⁻/h⁺ parting and migration capability of the HUCNs compared to

UCN. This is because of the availability of -OH groups at the edges of UCNs. These -OH groups can act as h+ scavengers to boost the separation of the photoinduced e⁻/h⁺ pairs. Moreover, a narrow nanofiber with a width of <50 nm will be advantageous for the electrons to migrate to the surface and increase the availability of active spots. The optimized PC could reduce 99.8% Cr(vi) compared to 30.8% of the pristine g-C₃N₄ catalyst under identical experimental conditions, such as the PC amount of 100 mg, $C_0 = 20 \text{ mg L}^{-1}$, volume = 100 mL, pH = 2.3 under artificial solar radiation. The reasons behind this exceptional photocatalytic reduction activity were as follows: The hydroxyl groups added to the HUCN's edges enhanced the contact between Cr(vI) and the HUCNs, helped to separate the charge carriers, and improved the accessibility of the active sites. Additionally, the HUCN's constructed nanostructure facilitated electron transfer to the PC surface, and the upward C_B edge potential gave the photoinduced electrons better reduction capability. The XPS spectrum of Cr 2p adsorbed on the 3.0-HUCN after the photocatalytic Cr(vi) remediation showed the presence of Cr(III), implying the conversion of Cr(VI), as shown in Fig. 8i.

Wei et al. subjected g-C₃N₄ to hydrothermal treatment in aqueous HNO3 solutions to modify the g-C3N4 morphology.89 The optimised PC showed improved reduction efficiency in comparison to untreated g-C3N4 towards the photocatalytic remediation of Cr(v_I). The greater photocatalytic Cr(v_I) remediation activity of the hydrothermally treated g-C3N4 was mainly due to their increased SSAs, smaller particle sizes and positive surface charges, causing boosted adsorption for Cr(v1). Other reasons were the more effective separation of photoinduced e⁻/ h⁺ pairs as well as the change in photocatalytic Cr(v_I) reduction mechanisms. The photocatalytic Cr(vI) reduction over untreated g-C₃N₄ was primarily via a two-step 'O₂ mediated indirect reduction mechanism. On the other hand, the same reaction over the hydrothermally treated g-C₃N₄ was through a one-step direct e reduction mechanism. The hydrothermal treatment appears to be a facile and useful way to enhance the Cr(v1) adsorption and photocatalytic remediation of g-C₃N₄.

Alam *et al.* fabricated an ACF-supported CoNiWO₄-g-C₃N₄ composite. Spectroscopic analytical methods were used to validate the creation of the Z-scheme-based CNW-g-C₃N₄ heterostructure on the ACF substrate. Under visible light irradiation, 98.2% degradation efficiency of Cr(vI) reduction at a concentration level of 200 mg L $^{-1}$ in 150 min, with a dose of 1 g L $^{-1}$ CNW-g-C₃N₄/ACF, could be achieved. The maximum reduction rate of CNW-g-C₃N₄/ACF is ascribed to the shared role of adsorption and photoreduction, in which the extensive absorption of visible light and improved charge separation efficiency played a crucial role. Five repeated cycles of use showed the catalyst stability.

Wang *et al.* constructed 2D/2D MoS₂/g-C₃N₄ heterostructures⁹¹ for photo-remediation of Cr(vI). From the TEM image in Fig. 9a, it may be seen that small flaky pieces of MoS₂ are evenly raised on the surface of large flaky g-C₃N₄. With an optimal composition denoted by MCN_{0.25}, Cr(vI) could be totally reduced to Cr(III) (100%) within 30 min under exposure to visible light at neutral pH (photocatalysts removal capacity 45

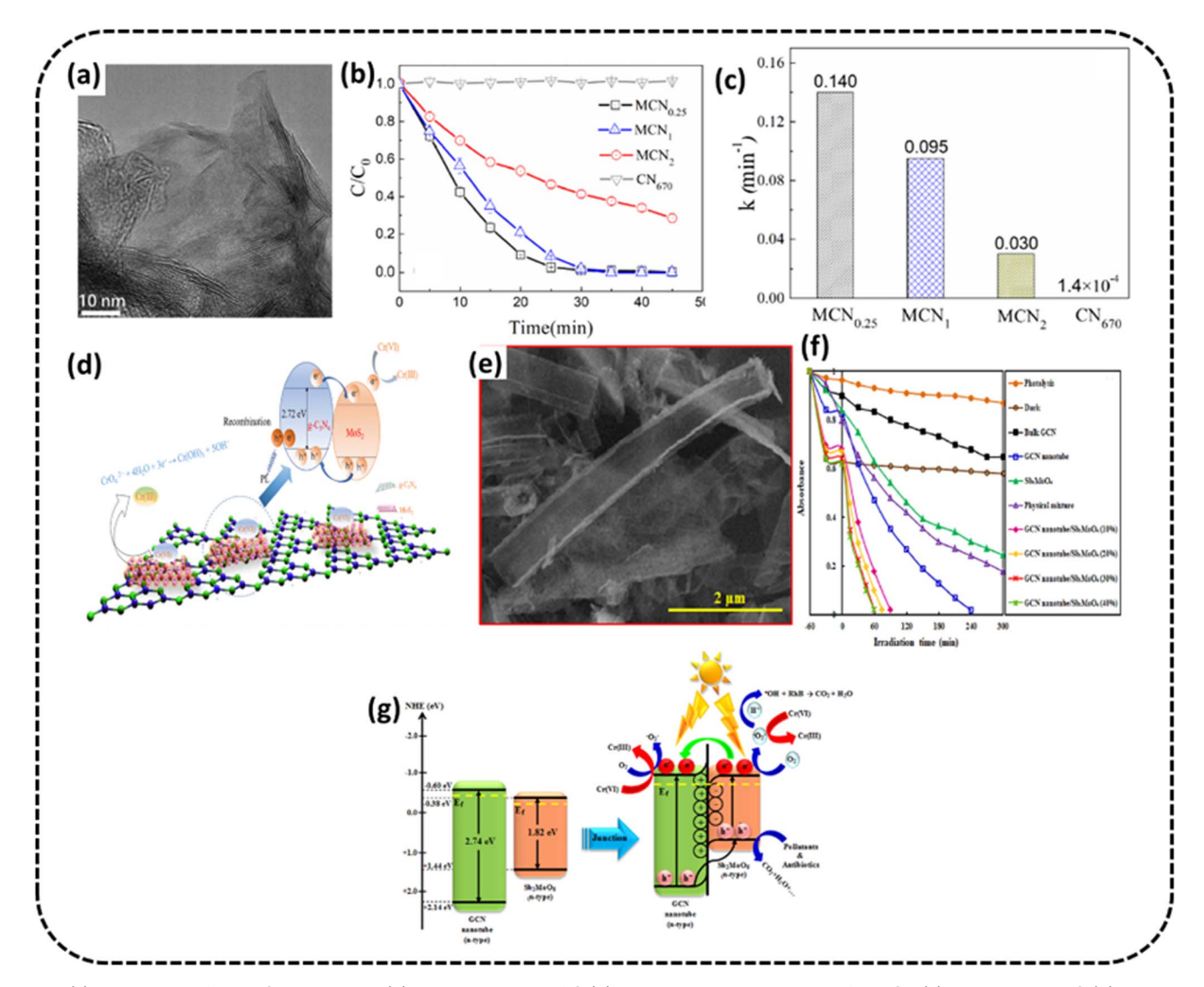


Fig. 9 (a) TEM image of the $MCN_{0.25}$ sample (b) variation curves of Cr(vi) concentration against time for MCN (c) photocatalytic Cr(vi) reduction rate for MCN (d) schematic of the mechanism of Cr(vi) photodegradation. Reproduced with permission from ref. 91 Copyright 2021, The American Chemical Society. (e) SEM images of the $g-C_3N_4$ nanotube/Sb₂MoO₆ (f) Cr(vi) removal rate over $g-C_3N_4$ nanotube/Sb₂MoO₆ (g) schematic for the mechanism of pollutant degradation of fabricated photocatalysts. Reproduced with permission from ref. 92, Copyright 2021, Elsevier.

mg g^{-1}), as shown in Fig. 9b. The rate constant of MoS₂/g-C₃N₄ composites and pristine g-C₃N₄ during photoreduction of Cr(v₁) are shown in the bar graph, which indicates the rate constant of MCN_{0,25} composite is about 1000 times more than pristine g-C₃N₄, as shown in Fig. 9c. This superior performance of PC was attributed to the chemical adsorption and photocatalytic reduction synergistically working together. Fig. 9d shows the reaction mechanism of Cr(vI) remediation from aqueous solution exposed to visible light helped by adsorption. Initially, Cr(v1), under chemisorption with MoS₂ grids, is attached to the surface of MCN. A type II heterojunction is created between MoS₂ with more positive conduction band potential compared to g-C₃N₄. The photogenerated electrons may be seen to migrate from the C_B of g-C₃N₄ to MoS₂, and holes moving from the V_B of MoS₂ to g-C₃N₄. The electrons on the C_B of MoS₂ then attack adsorbed Cr(vi) to convert to Cr(iii) efficiently.

Hemmati-Eslamlu *et al.* synthesized n-n heterojunctions fabricated from Sb_2MoO_6 and $g\text{-}C_3N_4$ nanotube.⁹² The SEM image of the nanotube formation is shown in Fig. 9e. The optimised photocatalyst $g\text{-}C_3N_4$ nanotube/ Sb_2MoO_6 (30%) sample was used for the photoreduction of Cr(vi) and the PC exhibited degradation efficiency 21.8 and 3.63-times more than that of bulk $g\text{-}C_3N_4$ and $g\text{-}C_3N_4$ nanotube samples, as shown in Fig. 9f. The probable charge migration route was suggested through the n-n heterojunction fabricated amid Sb_2MoO_6 and $g\text{-}C_3N_4$ nanotube, as shown in Fig. 9g. These remarkable photocatalytic improvements were credited to the boosted visible radiation absorption, fast separation of e^-/h^+ pairs and extended specific surface area.

Yuan *et al.* fabricated graphitic C_3N_4 nanosheets $(g-C_3N_4)/2$ ZnO amalgamated photocatalysts.⁹³ The rate of photocatalytic remediation of aqueous $Cr(v_1)$ was 18% and 34% for

Review

transfer for the reaction.

unadulterated g- $\mathrm{C_3N_4}$ and ZnO, respectively, under visible light for 240 min. The optimized PC could affect the photocatalytic reduction by 70% in 240 min while exposed to visible light. The PC could be recycled up to 5 times. The increased photoreduction of the g- $\mathrm{C_3N_4/ZnO}$ photocatalyst was attributed to the improved visible radiation absorption and actual split-up of photogenerated charge carriers at the interface and their

Abdel-Moniem *et al.* synthesized nanosheets of $(Bi_2S_3@gC_3N_4)$ by ultrasonication. The heterostructures of $Bi_2S_3@gC_3N_4$ NCs were checked for remediation of hexavalent chromium while exposed to visible light. The optimized photocatalyst $Bi_2S_3@g-C_3N_4$ displayed the best photoreduction activity, reaching 97% of $Cr(v_1)$ removal after 180 min under simulated solar light in the case of a 20 ppm $Cr(v_1)$ solution with 0.2 g L^{-1} of the photocatalyst. The high efficiency of the photocatalytic $Cr(v_1)$ reduction was attributed to the low combination rate of photogenerated charge carriers. The possibility of charge carrier recombination at both the surface and the bulk traps was reduced in $Bi_2S_3@g-C_3N_4$ nanosheets, improving the light utilization rate and increasing photocatalytic activity.

Chen *et al.* prepared porous nanosheets of g- C_3N_4 (PCN) with enhanced spacing⁹⁵ between layers and more SSA using a thermal polymerization method assisted by nickel. The surface of nanosheets had more exposed active sites, and its porosity helped in the movement of photons inside the lamellar structure, and therefore, enhanced efficacy in the absorption of visible radiation. The PCN thus obtained had a higher efficiency of photocatalytic $Cr(v_1)$ reduction than pristine g- C_3N_4 . The value of k, *i.e.*, the reaction rate constant of PCN (0.013 min⁻¹), was nearly two times that of pristine g- C_3N_4 (0.007 min⁻¹). The difference in the photocatalytic performance between PCN and g- C_3N_4 could be ascribed to higher SSA and the pores that increased absorption of visible light and a quicker path for transfer of photo-induced charges. The photo-induced e⁻was seen to be primarily responsible for $Cr(v_1)$ photocatalytic reduction. The PC could be recycled three times.

Chen et al. prepared ultrathin g-C₃N₄ nanosheets by exfoliation of raw g-C₃N₄ using edible glucose syrup.96 Compared to raw graphitic carbon nitride, the synthesized thin layers of g-C₃N₄ displayed an 18-fold improvement towards Cr(v₁) reduction, attributable to their greater SSA and more exposed active sites. Patnaik et al. synthesized bimetallic alloyed Au/Pd nanoparticles embedded on nanosheets of g-C₃N₄ modified by mesoporous silica with a not-so-complicated one-pot calcination method.97 The optimized CNM-AP nanocomposite could reduce $Cr(v_1) C_0 = 20 \text{ mg L}^{-1}$, catalyst concentration = 1 g mL⁻¹ to an extent of 56% under 2 h of visible light irradiation. As reallife wastewater streams contain organic materials that act as hole scavengers throughout the photocatalysis of Cr(vi) and boost the reduction reaction, the paper describes the remediation of Cr(v_I) in the presence of phenol. The catalyst was found to be stable enough to be recycled four times.

Element doping engineering

Ajiboye et al. fabricated silver functionalized g-C $_3N_4$ by calcinating g-C $_3N_4$ with AgNO $_3$. The TEM analysis displayed

a flower-like morphology for the Ag-doped g- C_3N_4 , as shown in Fig. 10a. The composite reduced 100 mg L^{-1} Cr(vI) at a low pH of value 2 to the extent of 35.3% in 120 min when exposed to visible light from a 28 W LED light, with a catalyst dosage of 50 mg. The degradation percentage was almost thrice as matched to pristine g- C_3N_4 (13.4%) (Fig. 10b). Under similar conditions, the PC could reduce 20 mg L^{-1} Cr(vI) to the extent of 67% in 120 min under visible light irradiation. The heightened photocatalytic activity of PC might be attributed to the decreasing rate of recombination of photogenerated e^-/h^+ pairs.

Xuan *et al.* prepared ruthenium-doped g- C_3N_4 .¹⁰⁰ The 5 percent Ru/g- C_3N_4 composite showed maximum photocatalytic activity. From the XPS analysis in Fig. 10c, the presence of Ru doping was evident with the Ru $3p_{3/2}$ peak values at 463.3 eV and 485.5 eV. At different concentrations of Cr(vi) (15–100 ppm) at a starting solution pH of 2.0 and catalyst concentration of 0.1 g L^{-1} with a reaction duration of 120 min, the photocatalytic efficacy of the Ru/g- C_3N_4 catalyst in the Cr(vi) reduction was studied. Up to 96.81% of available Cr(vi) could be reduced after 2 hours, which was twice better than the numbers for pristine g- C_3N_4 (50.1%). The PC could be recycled three times without loss of efficiency. The decrease in the photoinduced charge carrier recombination was identified as the cause of the increased efficacy of the Cr(vi) reduction using C_B electrons, which is schematically presented in Fig. 10d.

Masoumi Sangani *et al.*¹⁰¹ reported the synthesis of g- C_3N_4 modified with sulfanilic acid and loaded on chitosan beads (CS-GCN-S). The optimised photocatalyst of S-doped g- C_3N_4 nanosheets could display $Cr(v_1)$ reduction efficiency of greater than 90% within 180 min with catalyst quantity: 0.2 g L⁻¹, pH: 5, $Cr(v_1)$ initial concentration: 10 mgL⁻¹. The photocatalyst could be examined up to the fifth successive cycle without significant change in photocatalytic activity, implying its better stability and reusability.

Andreou et al. synthesized 2D/3D hybrid heterojunctions consisting of P-doped g-C₃N₄ nanosheets (~50-60 nm in adjacent size) and pint-sized Ni₂P nanoparticles of ~5-6 nm in radius99 and determined their noticeable performance in the photocatalytic Cr(vi) remediation. From the EIS studies, the excellent performance of PC could be ascribed to the Ni₂P alteration and P doping of the graphitic carbon nitride that improved the e⁻/h⁺ pair migration and spatial split-up through the boundary of Ni₂P/P-doped g-C₃N₄ junctions (smallest arc diameter) (Fig. 10e). Due to these alterations, the optimised PC having 15 wt% Ni₂P displayed better photocatalytic action in the remediation of aqueous effluents containing Cr(v1) under exposure to UV-visible radiation with 12.5% apparent quantum yield at 410 nm in the absence of sacrificial additives. PC stability was tested for three consecutive cycles. The PC could almost completely remove (>99%) (50 mg L⁻¹) Cr(v_I) solution in 50 min (PC concentration of 0.8 g L^{-1} at pH 1). In contrast, it took 3 h for ~44% and ~41% Cr(vi) remediation over g-C₃N₄ and P-g-C₃N₄ under identical conditions. The schematic in Fig. 10f shows the possible mechanism, depicting the migration of photoinduced electrons from the CB of graphitic carbon nitride to Ni₂P because of the inherent electric field created at

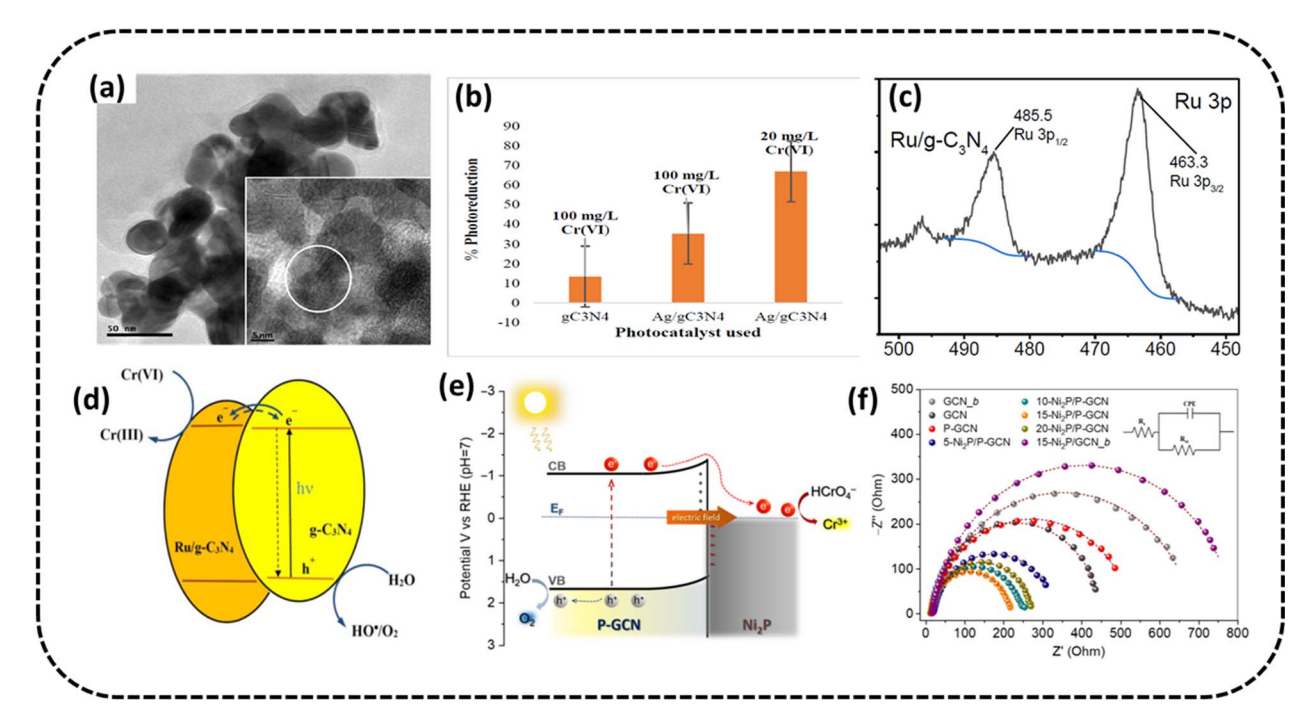


Fig. 10 (a) TEM image (inset HRTEM image) of Ag/g- C_3N_4 (b) bar graph displaying $Cr(v_1)$ reduction percentage at pH 2 under irradiation from a 28 W LED light. Reproduced with permission from ref. 98, Copyright 2022, Elsevier (c) XPS spectra of the Ru 3p scan of Ru/g- C_3N_4 (d) schematic of the charge-migration mechanism of the photocatalytic $Cr(v_1)$ remediation using ruthenium doped $g-C_3N_4$. Reproduced with permission from ref. 100, Copyright 2023, MDPI (e) suggested mechanism for the UV-vis generated photocatalytic $Cr(v_1)$ remediation over $Ni_2P/P-g-C_3N_4$ catalysts (f) Nyquist diagrams (inset: Randles equivalent circuit model). Reproduced with permission from ref. 99, Copyright 2023, MDPI.

the Ni_2P/P -g- C_3N_4 Schottky junctions, where the $Cr(v_1)$ manifested as $HCrO_4^-$ was effectively converted to Cr(III).

Jing Zhang *et al.*¹⁰² fabricated iron-doped graphitic carbon nitride loaded with modified dispersed diatomite. The optimal PC of 10% Fe composite with an EB dose of 30 kGy displayed improved remedial efficacy with 98.3% of available Cr(vi) in 100 min, which was nearly 16.92 times more than that of pristine $g\text{-}C_3N_4$. The PC displayed good stability even after using four times. The grand performance of PC could be attributed to Fe doping, which hindered the charge carrier recombination of photoinduced e^-/h^+ pairs and the capture of photoinduced carriers.

Shi *et al.*¹⁰³ prepared a photocatalytic coating of carbon nanotubes/sulphur doped carbon nitride composite sample (CNT/SCN) by a two-step solvothermal method. The prepared CNT/SCN coating demonstrated a better photocatalytic reduction efficacy of 84.7% for Cr(vI) (10 mg L^{-1}) within 8 hours under flowing water conditions. The reduction capability could surpass 75% even after three cycles of experimentation. Furthermore various other g-C₃N₄ modified photocatalytic systems engaged for Cr(vI) removal are summeried in table (Table 1).

Future prospective and conclusions

Photocatalytic $Cr(v_l)$ reduction is considered an effective strategy compared to conventional methods of redemption. g- C_3N_4 , being a non-metallic photocatalytic semiconductor

material, possesses wide application prospects in the photocatalytic arena owing to non-toxicity, high photocatalytic behavior, adequate electronic structure, visible light absorption capability, abundantly available precursors and costeffectiveness. This comprehensive review particularly focuses on the recent trend of photocatalytic Cr(vi) reduction using g-C₃N₄ along with the reaction mechanism. Although various modifications on g-C₃N₄ enhance chromium reduction remarkably, some lacunas still need to be addressed before being used in practical applications. The knowledge behind the reaction mechanism involved in photocatalytic chromium reduction is still insufficient. In order to explain the reaction mechanism taking place during the process of photocatalysis, free radical capturing experiments, RDE and ESR studies are usually preferred. The methods reported herein provide a routine understanding of the reactions and kinetics of the reactants that lack in-depth understanding. Therefore, new techniques like TPV, in situ XAS, and TPC can systematically elucidate the reaction procedures of Cr(vi) reduction at the molecular level.

While it is easier to augment the performance of the photocatalyst, designing active sites on it is quite tough. It is very difficult to control the atom vacancies, quantity of heteroatoms and emending active sites at the time of synthesis. Therefore, studies on developing advanced synthesis approaches should be prioritized for the preparation of $g\text{-}C_3N_4$, which can address the above-mentioned issues. The $g\text{-}C_3N_4$ production through the normal methods is still quite challenging and not

 $\textbf{Table 1} \quad \text{Summary of the numerous investigations on the removal of } Cr(v_1) \text{ using various } g-C_3N_4-\text{based nanocomposites}$

Sl. no.	Name of PC/nanocomposite	Reported Cr(vi) removal and PC stability. C_0 /ppm	References
1	g- C_3N_4 -n-p type ZnO/BiOBr heterojunction	99% $C_0 = 10$	72
		60 min	
2	CA-g-C ₃ N ₄ <i>i.e.</i> petal-like g-C ₃ N ₄ impregnated with	Four cycles 93%	84
_	citric acid (CA)	$C_0 = 20$	04
	cruite deta (ers)	Three cycles	
34	Ruthenium-modified g-C ₃ N ₄	96.8%	100
	- '	$C_0 = 20$	
		Three cycles	
4	$ m g ext{-}C_3N_4/HAP$	100%	85
		$C_0 = 40$	
		UV 25 vis 210 min	
5	$g-C_3N_4/Bi_2S_3$	Eight cycles 93.4%	73
6	Ag ₃ VO ₄ /g-C ₃ N ₄ /diatomite/DT	70%	104
o .	1153 1 04/5 03114/ diatorine (DI	Within 60 min	101
		Three cycles	
7	g-C ₃ N ₄ -nanosheet/ZnMoO ₄	100%	75
		$C_0 = 5$	
		120 min	
		Four cycles	
8	g - C_3N_4/Ag	67%	98
		$C_0 = 20 \text{ mg L}^{-1}$	
0	Constitution and an articular formation alice devicts the	120 min	105
9	Graphitic carbon nitride functionalized with the	92.77%	105
10	rod-like Cu _{3.21} Bi _{4.79} S ₉ ternary complex Ag ₂ O-Ag ₂ CO ₃ /g-C ₃ N ₄ (p-n/n-n dual	$C_0 = 10$ 89%	76
10	heterojunctions)	Five cycles	70
11	Ag ₃ PO ₄ /g-C ₃ N ₄	87.6%	74
12	g - C_3N_4 (c OH-CN) and g - C_3N_4 (c H-CN)	100% in 60 min	88
13	g-C ₃ N ₄ /ZnIn ₂ S ₄ nanocomposites	95%	106
		$C_0 = 100$	
		60 min	
		Five cycles	
14	g-C ₃ N ₄ photocatalysts using urea, thiourea.	99.5%	86
	Melamine and dicyandiamide as precursors	60 min	
	Bi ₂ S ₃ @g-C ₃ N ₄ nanosheets	UCN	
15		$C_0 = 10$	94
		180 min 67.1% vis 93.1% UV	
16	Porous graphitic carbon nitride	About 91%	95
10	1 orous grapinice carbon marac	90 min	55
		Three cycles	
17	Ultrathin g-C ₃ N ₄ nanosheets	18-Fold enhancement in Cr(v1) reduction	96
18	Au/Pd bimetallic alloyed nanoparticles decorated	$C_0 = 20$	97
	on mesoporous silica-modified g-C3N4 nanosheets	56% in 240 min	
		Four cycles	
19	Ag9NCs/g-C ₃ N ₄ and Ag32NCs/g-C ₃ N ₄ hybrid	$C_0 = 30$	82
	nanocomposites	100% in 50 min	
20	College War College Britanian College	Five cycles	
20	CoS ₂ /g-C ₃ N ₄ -rGO hybrid nanocomposites	99.8% 120 min	77
21	Hydroxyl-modified graphitic carbon nitride (HUCN)	Five cycles	87
	Tryatoxyt mounicu grapinuc carbon munuc (110CN)	99.8% 45 min Five cycles	07
22	$g\text{-}\mathrm{C}_3\mathrm{N}_4/\mathrm{polyvinylidene}$ fluoride composite	Alone mat 23%	107
_		$C_0 = 30$	
		240 min	
		85% with formic acid	
		Five cycles	
23	g - C_3N_4 / C / $BiFeO_3$	93%	108
24	g-C ₃ N ₄ @CA/B-PET where cellulose aerogel is CA,	200 mg of PC could reduce $Cr(v_I)$ (2 × 10 ⁻⁴ mol L ⁻¹)	83
	PET stands for polyethylene terephthalate	to the extent of 91% in 120 min under sunlight	

Table 1 (Contd.)

Sl. no.	Name of PC/nanocomposite	Reported Cr(v _I) removal and PC stability. C_0 /ppm	References
25	Pd nanocones supported on g-C ₃ N ₄	Up to 99.9%	109
	11 0 3 4	20 min	
		Five cycles	
26	Graphitic carbon nitride supported sulfur	99% in 15 min	110
	nanoparticles	$C_0 = 100$	
	•	30 mg PC	
		Seven cycles	
27	TiO ₂ /g-C ₃ N ₄ microspheres/reduced graphene oxide	97% after 240 min	111
		$C_0 = 100$	
		50 mg PC	
		Five cycles	
28	Ag_3PO_4/g - C_3N_4	94.1%	31
	03 40 3 4	Five cycles	
29	ACF-supported CoNiWO ₄ -g-C ₃ N ₄	98.2%	90
-	46.34	$C_0 = 200 \text{ ppm}$	
		150 min	
		$1~{ m g}~{ m L}^{-1}~{ m PC}$	
		Five cycles	
30	Iron-doped g-C ₃ N ₄ loaded with modified dispersed	98.3% of Cr(v1) in 100 min	102
- *	diatomite	Four cycles	
31	2D/3D Ni ₂ P/P-doped g-C ₃ N ₄	(>99%) (50 mg L ⁻¹) 50 min	99
	2 1 0 3 4	0.8 gL^{-1} PC at pH 1	
		Three cycles	
32	$2D/2D \text{ MoS}_2/\text{g-C}_3\text{N}_4$	(>99%)	90
		<30 min	
		PC removal capacity 45 mg g ⁻¹	
33	$\mathrm{Bi_4O_5I_2/g\text{-}C_3N_4}$	(90.3%)	79
	4-5-28 -5-4	$(40 \text{ mg L}^{-1}) 60 \text{ min}$	
		$0.4 \text{ g L}^{-1} \text{ PC at pH } 2.2$	
		Five cycles	
34	$2D/2D MoS_2/g-C_3N_4$	(>90%)	101
J4	25/25 11002/8 03114	$(10 \text{ mg L}^{-1}) 180 \text{ min}$	101
		0.2 gL^{-1} PC at pH 5	
		Five cycles	
35	CNT/sulphur doped g-C ₃ N ₄	(~85%)	103
00	Oliver print doped & Osliva	$(10 \text{ mg L}^{-1}) \text{ 8 hours}$	103
		Three cycles under flowing water conditions	
		Timee cycles under nowing water conditions	

recommended for various functionalizations because of the absence of abundant active sites required for surface chemical reactions. As there are a variety of strategies in the fabrication procedure of graphitic carbon nitride, with each approach altering the feature of the prepared g-C₃N₄, a pressing need to improvise these techniques via eco-friendly methods is essential. Doping Strategies like Elemental Doping that involve incorporating heteroatoms (such as N, B, S, P) into the g-C₃N₄ lattice can create active sites by changing the electronic structure. These dopants are capable of enhancing charge transfer and promoting specific surface reactions. Metal Doping: introducing metal atoms (e.g., Co, Ni, and Pt) onto the g-C₃N₄ surface can create catalytically active centers. These metals can serve as electron sinks on the catalyst surface, helping charge separation and supporting redox reactions. Defect Engineering: controlled introduction of defects (such as vacancies or edge sites) can create active sites. Defects modify the nearby electronic environment, making them more favorable for adsorption followed by the reaction. Edge Sites modification: increasing the edge-tobasal plane ratio exposes more active sites. Strategies like

exfoliation or edge-functionalization are capable of enhancing edge site density. Surface Functionalization: covalently attaching functional groups (*e.g.*,–NH₂, –OH) to the g-C₃N₄ surface can create active sites. These groups can participate in surface reactions.

 $Cr(v_1)$ reduction through three-electron oxygen reduction generally has high selectivity and the one-electron oxygen reduction path possesses a quicker rate of $Cr(v_1)$ reduction. Basically, both pathways are highly dependent on the capability of the photocatalyst to efficiently transfer e^- to O_2 . Introducing carbon vacancies for better absorption of O_2 by doping alkali metals for the generation of Lewis acid sites is quite helpful. However, there is no clear evidence about which modification is more favorable for $Cr(v_1)$ reduction and which functional group is helpful for participating in the reaction. Additionally, the perfect interpretation of the mechanistic approach can only be achieved based on theoretical calculations.

One of the prerequisites for the practical application of photocatalytic Cr(v1) remediation is the long-term stability of the photocatalyst. All the studies analyzing cycling plus aging tests

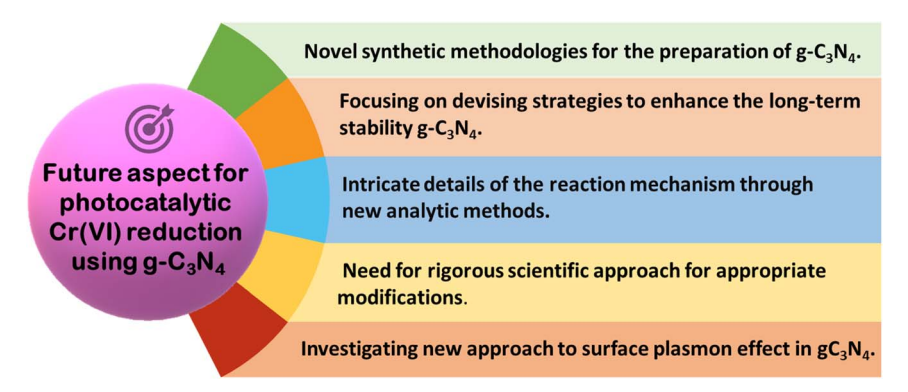


Fig. 11 Schematic depicting the future perspective of $q-C_3N_4$ -based photocatalysts towards chrome remediation.

on photocatalysts and XRD, XPS, TEM with other characterizations for used catalysts refer to their good stability, but the test duration is comparatively short. The short-term stability of the photocatalyst may be due to its deactivation with several test runs. Therefore, it is highly essential to pump the cycling ability as long as it can be. Specially, in the case of Cr(vI) remediation, higher efficiency can be attained by varying experimental conditions such as solution pH, catalyst amount, light intensity, temperature, irradiation time, sacrificial agent amount, Cr(vI) ion concentration and photocatalyst stability.

Another concept of the surface plasmon effect in g-C₃N₄ can also play a necessary role in enhancing photocatalytic Cr(v1) reduction. The phenomenon of collective oscillation of free electrons upon light illumination could drastically increase the reaction processes along with better light absorption and charge separation. Hence, more studies may be conducted in this context to augment photocatalytic Cr(v1) reduction via g-C₃N₄. This includes investigation of other materials like noble metals, metal oxides with tailored LSPR properties, exploration of hybrid systems (e.g., metal-semiconductor composites) to synergize LSPR with existing photocatalysts, optimization of the nanostructure design (size, shape, composition) to maximize LSPR effects, understanding the interplay between LSPR and charge carrier dynamics, studying LSPR-induced hot electrons and their role in redox reactions, and consideration of realworld applications, such as water purification or pollutant degradation.

This review is centered on work carried out so far using newage novel graphitic carbon nitride-based nanocomposites for $Cr(v_I)$ remediation using visible light. The conversation makes it abundantly evident that the majority of these photocatalyst materials are still in the early stages of investigation in the lab. These graphitic carbon nitride-based nanocomposites are yet to be used for practical purposes. Therefore, further research is required for real-life situations using actual wastewater containing $Cr(v_I)$ in different scales and continuous operation modes. In order to advance research towards a commercial-scale ETP, more studies are required to address the large-scale synthesis of nanomaterials, develop photo reactors of the proper size, and optimize the economy for processes based on g- C_3N_4 nanomaterials. As real-world applications involve complex

matrices, raw samples from polluted sites are required to be used in exploring field trials with g-C₃N₄ photocatalyst in a small solar pond. The results of the optimization study of trial runs in the pond should generate enough engineering data needed to design a pilot plant-scale reactor. Thereafter, the studies in pilot-scale plants are essential for validating catalyst performance based on which actual largescale plants may be designed and used. A summary regarding the highly required future perspective is presented in Fig. 11.

Abbreviations

ETP

2D	Two dimensional
3D	Three dimensional
Cr(vi)	Hexavalent chromium
Cr(iii)	Trivalent chromium
Cr(0)	Zerovalent or metallic chromium
CB	Conduction band
NPs	Nanoparticles
EA	Elemental analysis
XRD	X-ray powder diffraction
XPS	X-ray photoelectron spectroscopy
VB	Valance band
UVDRS	Ultraviolet-visible diffuse reflectance spectroscopy
PC	Photocatalyst
TEM	Transmission electron microscopy
SEM	Scanning electron microscope
PEC	Photoelectrochemical
h^{+}	Holes
e^{-}	Electron
$-\mathbf{O}_2^*$	Super oxide radical
-OH*	OH radical
ROS	Reactive oxidative species
ESP	Electrostatic potential
RDE	Rotating disk electrode
ESR	Electron spin resonance
TPV	Transient photovoltaic responses
XAS	X-ray absorption spectroscopy
TPC	Transient photo current measurement

Effluent treatment plant

RSC Advances Review

Data availability

Data will be available upon reasonable request.

Conflicts of interest

There are no conflicts to declare.

Acknowledgements

The authors are thankful to the S 'O' A (Deemed to be University) management for their constant support and motivation. Upali Aparajita Mohanty is grateful to UGC for the award of the SJSGC fellowship (UGCES-22-GE-ORI-F-SJSGC-5637).

References

- 1 L. J. D. Moreira, E. B. da Silva, M. P. F. Fontes, X. Liu and L. O. Ma, Environ. Pollut., 2018, 239, 384-391.
- 2 K. Nakamuro, K. Yoshikawa, Y. Sayato and H. Kurata, Mutat. Res. Genet. Toxicol., 1978, 58, 175-181.
- 3 A. Zhitkovich, Chem. Res. Toxicol., 2011, 24, 1617-1629.
- 4 Agency for Toxic Substances and Disease Registry, ATSDR's substance priority list, available www.atsdr.cdc.gov/.
- 5 D. Paustenbach, B. Finley, F. Mowat and B. Kerger, J. Toxicol. Environ. Health, Part A, 2003, 66(14), 1295-1339.
- 6 Z. Zhao, H. An, J. Lin, M. Feng, V. Murugadoss, T. Ding, H. Liu, Q. Shao, X. Mai, N. Wang, H. Gu, S. Angaiah and Z. Guo, Chem. Rec., 2019, 19, 873-882.
- 7 M. Kumari, C. U. Pittman Jr and D. Mohan, J. Colloid Interface Sci., 2015, 442(15), 120-132.
- 8 D. K. Padhi, A. Baral, K. Parida, S. K. Singh and M. K. Ghosh, J. Phys. Chem. C, 2017, 121(11), 6039-6049.
- 9 D. Kandi, S. Martha, A. Thirumurugan and K. M. Parida, ACS Omega, 2017, 2(12), 9040-9056.
- 10 R. Acharya, B. Naik and K. Parida, Beilstein J. Nanotechnol., 2018, 9, 1448-1470.
- 11 P. Babu, S. Mohanty, B. Naik and K. Parida, Inorg. Chem., 2019, 58(18), 12480-12490.
- 12 K. K. Das, S. Patnaik, B. Nanda, A. C. Pradhan and K. Parida, ChemistrySelect, 2019, 4(5), 1806-1819.
- 13 L. Sun, P. Li, Z. Shen, Y. Pang, X. Ma, D. Qu, L. An and Z. Sun, Adv. Energy Sustainability Res., 2023, 4(11), 2300090.
- 14 R. Xue, C. Huang, J. Deng, L. Yang, L. Li and X. Fan, J. Mater. Chem. A, 2022, 10, 3771-3781.
- 15 X. Wang, K. Maeda, A. Thomas, K. Takanabe, G. Xin, J. M. Carlsson, K. Domen and M. Antonietti, Nat. Mater., 2009, 8(1), 76-80.
- 16 F. P. Filice, J. D. Henderson, M. S. M. Li and Z. Ding, ACS Omega, 2019, 4(1), 2142-2151.
- 17 S. S. Wise and J. P. Wise, Sr, *Mutat. Res.*, 2012, 733(1), 78–82.
- 18 Q. Y. Chen, A. Murphy, H. Sun and M. Costa, Toxicol. Appl. Pharmacol., 2019, 377, 114636.
- 19 K. P. Nickens, S. R. Patierono and S. Ceryak, Chem. Biol. Interact., 2010, 188(2), 276-288.

- 20 A. W. Parvaze, J. A. Wani and S. Wahid, J. Environ. Chem. Eng., 2018, 6(4), 3798-3807.
- 21 S. Ali, R. A. Mir, A. Tyagi, N. Manzar, A. S. Kashyap, M. Mushtaq, A. Raina, S. Park, S. Sharma, A. M. Zahoor, S. A. Lone, A. A. Bhat, U. Baba, H. Mahmoudi and H. Bae, Plants, 2023, 12(7), 1502.
- 22 R. Jobby, P. Jha, A. K. Yadav and N. Desai, J. Plant Interact., 2018, 207, 255-266.
- 23 A. Bhati, S. R. Anand, D. Saini and S. K. Sonkar, npj Clean Water, 2019, 2, 1-9.
- 24 Y. Zhang, M. Xu, H. Li, H. Ge and Z. Bian, Appl. Catal., B, 2018, 226, 213-219.
- 25 R. Djellabi, P. Su, E. A. Elimian, V. Poliukhova, S. Nouacer, I. A. Abdelhafeez, N. Abderrahim, D. Aboagye, V. V. Andhalkar, W. Nabgan, S. Rtimi and S. Contreras, J. Water Process Eng., 2022, 50, 103301.
- 26 J. J. Testa, M. A. Grela and M. I. Litter, Langmuir, 2001, 17, 3515-3517.
- 27 J. J. Testa, M. A. Grela and M. I. Litter, Environ. Sci. Technol., 2004, 38, 1589-1594.
- 28 J. Djellabi, J. Ali, M. Yang, R. Haider, P. Su, C. L. Bianchi and X. Zhao, Sep. Purif. Technol., 2020, 250, 116954.
- 29 R. Djellabi and M. F. Ghorab, Desalin. Water Treat., 2015, 55, 1900-1907.
- 30 B. A. Marinho, R. O. Cristóvão, R. Djellabi, J. M. Loureiro, R. A. Boaventura and V. J. P. Vilar, Appl. Catal., B, 2017, 203, 18-30.
- 31 D.-S. An, H.-Y. Zeng, G. F. Xiao, J. Xiong, C.-R. Chen and G. Hu, J. Taiwan Inst. Chem. Eng., 2020, 117, 133-143.
- 32 V. Hasija, P. Raizada, P. Singh, N. Verma, A. Khan, A. Singh, R. Selvasembian, S. Y. Kim, C. Hussain, V.-H. Nguyen and Q. Le, Process Saf. Environ. Prot., 2021, 152, 663-678.
- 33 M. Valari, A. Antoniadis, D. Mantzavinos and I. Poulios, Catal. Today, 2015, 252, 190-194.
- 34 Y. Jinghai, W. Xingtong, L. Xuefei, L. Yang, G. Ming, L. Xiaoyan, K. Lingnan and Y. Suyang, Appl. Phys. A, 2011, 105(1), 161-166.
- 35 E. G. Gillan, Chem. Mater., 2000, 12(12), 3906-3912.
- 36 Y. Zhang and M. Antonietti, Chem. Asian J., 2010, 5(6), 1307-1311.
- 37 G. Dong, Y. Zhang, Q. Pan and J. Qiu, J. Photochem. Photobiol. C Photochem. Rev., 2014, 20, 33-50.
- 38 A. Thomas, A. Fischer, F. Goettmann, M. Antonietti, J.-O. Müller, R. Schlögl and J. M. Carlsson, J. Mater. Chem., 2008, 18(41), 4893-4908.
- 39 F. Dong, L. Wu, Y. Sun, M. Fu, Z. Wu and S. C. Lee, J. Mater. Chem., 2011, 21, 15171-15174.
- 40 Y. Zhang, J. Liu, G. Wu and W. Chen, *Nanoscale*, 2012, 4(17), 5300-5303.
- 41 L. Stradella and M. Argentero, Thermochim. Acta, 1993, **219**(27), 315-323.
- 42 S. P. Pattnaik, A. Behera, S. Martha, R. Acharya and K. M. Parida, J. Mater. Sci., 2019, 54(7), 5726-5742.
- 43 S. P. Pattnaik, A. Behera, R. Acharya and K. M. Parida, J. Environ. Chem. Eng., 2019, 7(6), 103456.
- 44 S. Patnaik, K. K. Das, A. Mohanty and K. M. Parida, Catal. Today, 2018, 315, 52-66.

Review

45 K. K. Das, S. Patnaik, S. Mansingh, A. Behera, A. Mohanty, C. Acharya and K. M. Parida, *J. Colloid Interface Sci.*, 2020, **561**, 551–567.

- 46 S. Patnaik, D. P. Sahoo and K. M. Parida, *Mater. Today Proc.*, 2021, 35, 247–251.
- 47 P. Babu, S. Mohanty, B. Naik and K. M. Parida, *ACS Appl. Energy Mater.*, 2018, **1**(11), 5936–5947.
- 48 S. Nayak and K. M. Parida, ACS Omega, 2018, 3(7), 7324-7343.
- 49 S. Patnaik, S. Martha, G. Madras and K. M. Parida, *Phys. Chem. Chem. Phys.*, 2016, **18**, 28502–28514.
- 50 A. Sattler, S. Pagano, M. Zeuner, A. Zurawski, D. Gunzelmann, J. Senker, K. Müller-Buschbaum and W. Schnick, *Chem.-Eur. J.*, 2009, 15(47), 13161–13170.
- 51 S. C Yan, Z. S. Li and Z. G. Zou, *Langmuir*, 2009, **25**(17), 10397–10401.
- 52 X. Li, J. Zhang, L. Shen, Y. Ma, W. Lei, Q. Cui and G. Zou, *Appl. Phys. A*, 2009, **94**, 387–392.
- 53 G. Dong, W. Ho, Y. Li and L. Zhang, *Appl. Catal., B*, 2015, 174–175, 477–485.
- 54 J. Fang, H. Fan, M. Li and C. Long, J. Mater. Chem. A, 2015, 3, 13819–13826.
- 55 M. Sahoo, P. Babu, C. P. Singh, S. Krishnamurthy and K. M. Parida, J. Alloys Compd., 2022, 898, 162853.
- 56 L. Ge, F. Zuo, J. Liu, Q. Ma, C. Wang, D. Sun, L. Bartels and P. Feng, J. Phys. Chem. C, 2012, 116(25), 13708–213714.
- 57 H. Lan, L. Li, X. An, F. Liu, C. Chen, H. Liu and J. Qu, *Appl. Catal.*, B, 2017, 204, 49–57.
- 58 K. Maeda, X. Wang, Y. Nishihara, D. Lu, M. Antonietti and K. Domen, *J. Phys. Chem. C*, 2009, **113**, 4940–4947.
- 59 J. Liu, H. Wang, Z. P. Chen, H. Moehwald, S. Fiechter, R. vande Krol, L. Wen, L. Jiang and M. Antonietti, Adv. Mater., 2015, 27, 712–718.
- 60 T. Tyborski, C. Merschjann, S. Orthmann, F. Yang, M. C. Lux-Steiner and T. Schedel-Niedrig, J. Phys.: Condens. Matter, 2012, 24(16), 162201.
- 61 Q. Han, B. Wang, J. Gao, Z. Cheng, Y. Zhao, Z. Zhang and L. Qu, ACS Nano, 2016, 10, 2745–2751.
- 62 P. Yang, H. Ou, Y. Fang and X. Wang, *Angew. Chem., Int. Ed.*, 2017, **56**, 3992–3996.
- 63 J. Oh, R. J. Yoo, S. Y. Kim, Y. J. Lee, D. W. Kim and S. Park, *Chem. Eur J.*, 2015, **21**(16), 6241–6246.
- 64 Y. Su, Y. Zhang, X. Zhuang, S. Li, D. Wu, F. Zhang and X. Feng, *Carbon*, 2013, **62**, 296–301.
- 65 X. Li, J. Zhang, Y. Huo, K. Dai, S. Li and S. Chen, *Appl. Catal.*, *B*, 2021, **280**, 119452.
- 66 S. Patnaik, G. Swain and K. M. Parida, *Nanoscale*, 2018, 10, 5950–5964.
- 67 J. Yu, K. Wang, W. Xiao and B. Cheng, *Phys. Chem. Chem. Phys.*, 2014, 16, 11492–11501.
- 68 H. Yu, R. Shi, Y. Zhao, T. Bian, Y. Zhao, C. Zhou, G. I. N. Waterhouse, L.-Z. Wu, C. H. Tung and T. Zhang, Adv. Mater., 2017, 29, 1605148.
- 69 Y. Zheng, Z. Zhang and C. Li, J. Mol. Catal. A: Chem., 2016, 423, 463–471.
- 70 B. Rhimi, C. Wang and D. W. Bahnemann, *J. Phys.: Energy*, 2020, 042003.

- 71 J. Zhang, Y. Hu, X. Jiang, S. Chen, S. Meng and X. Fu, *J. Hazard. Mater.*, 2014, **280**, 713–722.
- 72 T. X. Q. Nguyen, S.-S. Chen, M. Pasawan and H.-M. Chang, *Environ. Technol. Innovat.*, 2023, 103154.
- 73 L. Ding, Y. Deng, X. Liu, L. Liu, J. Ding and F. Deng, *J. Chem. Eng. Res. Updates*, 2022, **9**, 1–12.
- 74 T. Yang, P. Deng, L. Wang, J. Hu, Q. Liu and H. Tang, *Chin. J. Struct. Chem.*, 2022, 41(6), 2206023–2206030.
- 75 M. Mousavi, S. Moradian, P. Pourhakkak, G. Zhang, M. M. Habibi, M. Madadi and J. Ghasemi, *Mater. Sci.*, 2022, 57, 9145–9163.
- 76 O. M. Bankole, K. I. Ojubola, O. S. Adanlawo, K. A. Oluwafemi, O. Adeola, A. O. Adedapo, M. A. Adeyemo, S. E. Olaseni, N. A. Oladoja, E. J. Olivier, E. E. Ferg and A. S. Ogunlaja, *J. Photochem. Photobiol., A*, 2022, 427, 113800.
- 77 Y. Wanga, S. Baoa, Y. Liub, W. Yanga, Y. Yua, M. Fengc and K. Lid, *Appl. Surf. Sci.*, 2020, **510**, 145495.
- 78 C. V. Reddy, K. R. Reddy, R. R. Zairov, B. Cheolho and J. Shim, *J. Environ. Manage.*, 2022, 315, 115120.
- 79 S. Mishra, L. Acharya, B. Marandi, K. Sanjay and R. Acharya, *Diam. Relat. Mater.*, 2024, **142**, 110834.
- 80 L. Zhao, L. Guo, Y. Tang, J. Zhou and B. Shi, *Ind. Eng. Chem. Res.*, 2021, **60**(37), 13594–13603.
- 81 H. Huo, X. Hu, H. Wang, J. Li, G. Xie, X. Tan, Q. Jin, D. Zhou, C. Li, G. Qiu and Y. Liu, *Int. J. Environ. Res. Publ. Health*, 2019, 16(17), 321.
- 82 X. Niu, J. Dong, X. Wang and Y. Yao, *Environ. Sci.: Nano*, 2020, 7, 2823.
- 83 S. Chen, W. Lu, J. Han, H. Zhong, T. Xu, G. Wang and W. Chen, *Chem. Eng. J.*, 2019, **359**, 119–129.
- 84 H. Yu, Q. Ma, C. Gao, S. Liao, Y. Zhang, H. Quan and R. Zhai, *Catalysts*, 2023, **13**, 641.
- 85 Y. Jiménez-Floresa, K. Jiménez-Rangela, J. E. Samaniego-Beníteza, L. Lartundo-Rojasd, H. A. Calderóne, R. Gómezb and A. Mantillaa, *Catal. Today*, 2022, **388–389**, 1168–1175.
- 86 J. Liang, C. Jing, J. Wang and Y. Men, *Molecules*, 2021, **26**(22), 7054.
- 87 X. Wang, L. Li, J. Meng, P. Xia, Y. Yang and Y. Guo, *Appl. Surf. Sci.*, 2020, **506**, 144181.
- 88 H. Sun, L. Wang, Y. Liu, Z. Cheng, Y. Zhao, H. Guo, G. Qu, T. Wang and X. Yin, *J. Environ. Manage.*, 2022, 15(324), 116431.
- 89 H. Wei, Q. Zhang, Y. Zhang, Z. Yang, A. Zhu and D. D. Dionysiou, *Appl. Catal.*, *A*, 2016, **521**, 9–18.
- U. Alam, K. Pandey and N. Verma, *Chemosphere*, 2022, 297, 134119.
- 91 C. Wang, G. Yang, W. Shi, K. Matras-Postolek and P. Yang, *Langmuir*, 2021, 37, 6337–6346.
- 92 P. Hemmati-Eslamlu, A. Habibi-Yangjeh, S. Asadzadeh-Khaneghah, H. Chand and V. Krishnan, *Adv. Powder Technol.*, 2021, 32, 2322–2335.
- 93 X. Yuan, C. Zhou, Q. Jing, Q. Tang, Y. Mu and A. Du, *Nanomaterials*, 2016, **6**(9), 173.
- 94 S. M. Abdel-Moniem, M. A. El-Liethy, H. S. Ibrahim and M. E. M. Ali, *Ecotoxicol. Environ. Saf.*, 2021, 226, 112808.

95 X. Chen, Y. Zhang, D. Yuan, W. Huang, J. Ding, H. Wan, W.-L. Dai and G. Guan, J. Mater. Sci. Technol., 2021, 71(30), 211–220.

RSC Advances

- 96 K. Chen, P. Ye, Y. Zhang, Y. Yuanyue, Y. Wu, Y. Cheng, S. Gong, S. Zhou and K. Xiao, *Nanotechnology*, 2021, 32(46), 465603.
- 97 S. Patnaik, D. P. Sahoo and K. M. Parida, *J. Colloid Interface Sci.*, 2020, **560**, 519–535.
- 98 T. O. Ajiboye, E. E. Imade, O. A. Oyewo and D. C. Onwudiwe, *J. Photochem. Photobiol.*, 2022, **432**, 114107.
- 99 E. K. Andreou, E. D. Koutsouroubi, I. Vamvasakis, S. Gerasimos and G. S. Armatas, *Catalysts*, 2023, **13**, 437.
- 100 T. N. Xuan, D. N. Thi, T. N. Ngoc, K. D. Quoc, M. Németh, S. Shoaib Mukhtar and O. Horváth, *Catalysts*, 2023, 13(6), 964.
- 101 Md. M. Sangani, Md. S. Shahin, Md A. Yavari, M. Faghihinezhad and M. Baghdadi, J. Ind. Eng. Chem., 2023, 130, 412-424.
- 102 J. Zhang, X. Zhang, T. Zhou, Y. Huang, L. Zhao, Z. Ren, X. Liu, L. Chen, Y. Shao, X. Ma, X. Xie and Z. Wu, J. Clean. Prod., 2021, 315, 128219.

- 103 Z. Shi, L. Rao, P. Wang and Y. Yu, Multilevel Immobilized Cnt/Scn Composite Photocatalytic Coating and its Efficient Adsorption and Reduction Over Cr(vi) Under Flowing Water Condition.
- 104 Z. Jiang, H. Zhu, W. Guo, Q. Ren, Y. Ding, S. Chen, J. Chen and X. Jia, *RSC Adv.*, 2022, **12**, 7671–7679.
- 105 T. O. Ajiboye, O. A. Oyewo, R. Marzouki and D. C. Onwudiwe, *Catalysts*, 2022, 12(10), 1075.
- 106 L. Yang, J. Zhao, Z. Wang, L. Wang, Z. Zhao, S. Li, G. Li and Z. Cai, *Spectrochim. Acta, Part A*, 2022, **276**(5), 121184.
- 107 D. Saha, T. J. Hoinkis and S. E. Van Bramer, *J. Colloid Interface Sci.*, 2020, 575, 433–442.
- 108 H. Huo, X. Hu, H. Wang, J. Li, G. Xie, X. Tan, Q. Jin, D. Zhou, C. Li, G. Qiu and Y. Liu, *Int. J. Environ. Res. Publ. Health*, 2019, 16(17), 3219.
- 109 J.-H. Wu, F.-Q. Shao, X.-Q. Luo, H.-J. Xu and A.-J. Wang, *Appl. Surf. Sci.*, 2019, 471, 935–942.
- 110 O. M. Bankole, D. T. Olorunsola and S. A. Ogunlaja, *J. Photochem. Photobiol.*, *A*, 2021, **405**, 112934.
- 111 G. Li, Y. Wu, M. Zhang, B. Chu, W. Huang, M. Fan, L. Dong and B. Li, *Ind. Eng. Chem. Res.*, 2019, **58**, 8979–8989.